

Multi-phase environment of Centaurus A galaxy

A. Borkar,¹★ T. P. Adhikari,²† A. Różańska,³ A. G. Markowitz,^{3,4} P. Boorman,^{1,5}
 B. Czerny,⁶ G. Migliori,^{7,8} B. De Marco,³ and V. Karas¹

¹ Astronomical Institute, Czech Academy of Sciences, Boční II 1401, 141 00 Prague, Czech Republic

² Inter University Centre for Astronomy and Astrophysics (IUCAA), Post Bag 4, Pune University Campus Ganeshkhind, Pune – 411007, Maharashtra, India

³ Nicolaus Copernicus Astronomical Center Polish Academy of Sciences, Bartycka 18, 00-716 Warsaw, Poland

⁴ University of California, San Diego, Center for Astrophysics and Space Sciences, 9500 Gilman Dr, La Jolla, CA 92093-0424, USA

⁵ Department of Physics & Astronomy, University of Southampton, SO17 1BJ, Southampton, United Kingdom

⁶ Center for Theoretical Physics, Polish Academy of Sciences, Al. Lotników 32/46, 02-668 Warsaw, Poland

⁷ Dipartamento di Fisica e Astronomia, Università di Bologna, viale Berti Pichat 6/2, 40127 Bologna, Italy

⁸ INAF - Istituto di Radioastronomia, Via P. Gobetti, 101 40129 Bologna, Italy

Accepted XXX. Received YYY; in original form ZZZ

ABSTRACT

We study the multi-phase medium in the innermost regions of the Centaurus A (Cen A) galaxy. Combined high-resolution observations with the ALMA and *Chandra* observatories indicate that the hot X-ray emitting plasma coexists with the warm and cold medium in Cen A. This complex environment is a source of CO lines with great impact for its diagnostics. We show the images from the two mentioned instruments covering the nuclear region (diameter of 10'' or ~ 184 pc), and we study the conditions for plasma thermal equilibrium and possible coexistence of cool clouds embedded within the hot X-ray emitting gas. Further, we demonstrate that the multi-phase medium originates naturally by the thermal instability arising due to the interaction of the high-energy radiation field from the nucleus with the ambient gas and dust. We show that cold gas clouds can coexist in the mutual contact with hot plasma, but even colder dusty molecular clouds have to be distanced by several hundred pc from the hot region. Finally, we propose a 3-D model of the appearance of the hot plasma and the CO line-emitting regions consistent with the *Chandra* image and we derive the integrated emissivity in specific molecular lines observed by ALMA from this model. To reproduce the observed images and the CO line luminosity the dusty shell has to be 419 pc thick and located at 1020 pc from the centre.

Key words: galaxies: active – galaxies: individual: Centaurus A – Galaxy: nucleus – instabilities

1 INTRODUCTION

Centaurus A (NGC 5128, Cen A) is a nearby galaxy with redshift $z = 0.00183$, located at a distance $D = 3.8 \pm 0.1$ Mpc (Harris et al. 2010). Being the nearest radio-loud active galactic nucleus, Cen A has played a major role in our understanding of the nature of accreting supermassive black holes (SMBH), circumnuclear environments, connections between active nuclei and host galaxies, and jet ejection and emission processes. Our knowledge of Cen A thus forms a template for studying active galactic nuclei (AGN) at farther distances, including radio-loud AGN and other gas-rich ellipticals. Cen A is also considered to be a prototypical FR I object (Fanaroff & Riley 1974).

Key insights have come from high-spatial resolution imaging with e.g., *Chandra X-ray Observatory*, very long baseline interferometry (VLBI), and the Atacama Large Millimeter/Submillimeter Array (ALMA) and include e.g., small-scale spectral and kinematic behaviour of jet components (e.g. Tingay et al. 2001; Hardcastle et al. 2007; Worrall et al. 2008; Goodger et al. 2010; Snios et al. 2019); interactions of jet ejecta and the interstellar medium (Kraft et al. 2003; Croston et al. 2009); hot interstellar medium and non-hydrostatic motions (Kraft et al. 2008); interaction of jet ejecta with stars or gas clouds in the host galaxy: (Hardcastle et al. 2003; Tingay & Lenc 2009); identification of numerous individual X-ray point sources, including X-ray binaries (Burke et al. 2013); and morphology and kinematics of circumnuclear molecular gas, including disk-like structures, at scales of tens to hundreds of parsecs (Neumayer et al. 2007; Espada et al. 2009, 2010). For a review

* E-mail: abhijeet.borkar@asu.cas.cz

† E-mail: tek@iucaa.in

of the host galaxy properties, nucleus, radio lobes, and links to suspected past major mergers, see e.g. Israel (1998).

A key part of forming this knowledge-template is discerning the ionization structure, dust content, and gas-dust interactions, particularly given the co-spatiality of the X-ray-emitting plasma and cold molecular clouds. The presence of an AGN provides a positive and negative feedback, creating a complex interstellar environment. Cen A possesses a dust lane which provides a large gas reservoir that can be funnelled towards the central black hole to fuel accretion. The central engine in turn influences the central region with outflows and the jet that drive the gas away, which can lead to formation of a multi-phase environment in the vicinity of the SMBH.

In this paper, we study the condition for the thermal instability (hereafter TI) and see how it shapes the multi-phase gas within 10" of the SMBH. At such a small distance, the nucleus of Cen A can be observed with high spatial resolution, thus giving us an insight into the plasma conditions under the combined influence of an active nucleus and a compact stellar cluster. Such observations were performed with the *Chandra* satellite in the soft X-ray band and with ALMA at millimetre wavelengths. We reconstruct images of the hot diffused plasma overlapping cold molecular gas on the diameter of 10" in the best known spatial resolution for both energy bands. Observations used in this paper were taken by ALMA in 2015-2016, and by *Chandra* in 2017.

Based on the ALMA and *Chandra* images, in the present paper we concentrate on the inner 10" region corresponding to $\sim 6 \times 10^{20}$ cm, i.e. ~ 180 pc, of Cen A, and on the fact that hot X-ray emitting plasma may coexist there with cold gas or molecular clouds. We study the condition of TI around the nucleus and see how it shapes the multi-phase gas in the close environment of the SMBH in comparison with what is actually observed. For this purpose we use photoionization calculations by the CLOUDY code¹, version 17.01 (Ferland et al. 2017), which calculates the transfer of radiation through the matter for a wide range of temperature and density, and for different shapes of illuminating radiation. We follow the approach presented by us in the cases of the Sagittarius A* (Sgr A*) SMBH at the centre of the Milky Way (Czerny et al. 2013; Kunneriath et al. 2014), and in the ultra-compact dwarf galaxy M60-UCD1 (Różańska et al. 2014, 2017).

The structure of this paper is as follows. In Sec. 2 we describe the current knowledge of the main properties of Cen A based on the large collection of data from different instruments. In the same section, we present ALMA and *Chandra* data used in this paper to follow the distribution of matter from high resolution images. Furthermore, we discuss the radiation field and luminosities collected from available observations of the Cen A nucleus, needed as an input for our photoionization modeling. The set-up of the model including the description of parameters used in our numerical calculations is presented in Sec. 3. All results are shown in Sec. 4. The comparison to observations and potential ways to generalize our scenario are discussed and concluded in Sec. 5.

2 OBSERVATIONS

2.1 Main properties of Cen A

The mass of the central black hole of Cen A determined by using gas neutral hydrogen H₂ kinematics spans typically best-fit values of $4.5 - 11 \times 10^7 M_{\odot}$ (Marconi et al. 2006; Krajnović et al. 2007;

¹ www.nublado.org

Neumayer 2010) and by using stellar kinematics spans values of $\sim 5.5 - 20 \times 10^7 M_{\odot}$ (Silge et al. 2005; Cappellari et al. 2009).

The observed activity of the Cen A nucleus is rather low. The Bondi accretion rate was estimated to be $\dot{M} = 6.4 \times 10^{-4} M_{\odot} \text{ yr}^{-1}$ (Evans et al. 2004). A number of long (~ 100 ks) *Chandra* exposures have allowed to identify several features such as an extended jet (Hardcastle et al. 2007; Worrall et al. 2008; Goodger et al. 2010; Snios et al. 2019), the radio-lobe shock (Croston et al. 2009), and numerous individual X-ray sources like X-ray binaries (Burke et al. 2013).

The extended diffuse X-ray emitting gas up to 6 kpc also pervades the nuclear region (Kraft et al. 2008). ALMA observations revealed a complex structure of this gas-rich elliptical galaxy, consisting of a circumnuclear disk, and molecular arms stretching out to dust lanes (McCoy et al. 2017). The study of emission lines has allowed the determination of the kinematics of the cold medium, suggesting some infall towards the nucleus (Espada et al. 2017).

To study the physical processes in the central region of Cen A, we need both high resolution images in different energy bands displaying spatial distribution of hot and cold gas around nucleus, and the broadband spectral energy distribution (SED) of the emission from the innermost region. The high resolution images provide the estimation of distances at which hot and cold emission is detectable and where the emitting material is located. A realistic source SED is used as an input for the photoionization calculations as described in Sec. 3. Furthermore, to properly estimate the total cooling and heating due to all radiative processes, including photoionization, an accurate estimation of the value of bolometric luminosity is required, which is taken into account by CLOUDY code. All those properties of Cen A are collected in this section.

2.2 ALMA millimeter data

To follow the distribution of the nuclear matter in the vicinity of the SMBH, we used the ALMA band 3 and 6 observations made towards the central region of Cen A obtained in the Cycle 3 observation campaign under the project 2015.1.00483.S (PI: F. Israel). The observations were carried out between December 2015 and August 2016 with multiple executions of the schedule blocks with the ALMA 12-m main array and the 7-m compact array (ACA). The main array observations were made with 34 – 46 antennas, while the ACA with 11 antennas, providing the unprojected baseline lengths between 15 to 1500 metres for the main array and 8–43 metres for the ACA. The primary beam (field of view) obtained for the 12-m antenna is $\sim 53''$ (954 pc) for band 3 and $23''$ (414 pc) for band 6, and $91''$ (1.6 kpc) for the 7-m ACA antenna. The maximum recoverable scale ($\sim 124'' \times (1m/D_{\min}) \times (300 \text{ GHz}/\nu)$, where D_{\min} is the minimum baseline in metres and ν the observation frequency in GHz), is $22''$ (396 pc) for band 3 and $9''$ (162 pc) for band 6 with the main array and $40''$ (720 pc) for band 3 with the ACA.

The observations were aimed at detecting line emission from ¹²CO, ¹³CO, C¹⁸O, CS, HCN, HCO+ and HNC molecules in the central region of Cen A. The CO (1–0) ($\nu_{\text{rest}} = 115.27$ GHz), ¹³CO (1–0) ($\nu_{\text{rest}} = 110.20$ GHz), C¹⁸O (1–0) ($\nu_{\text{rest}} = 109.78$ GHz), and CS (2–1) ($\nu_{\text{rest}} = 97.98$ GHz) line emission was detected in band 3, and HCN (3–2) ($\nu_{\text{rest}} = 265.88$ GHz), HCO+ (3–2) ($\nu_{\text{rest}} = 267.56$ GHz) and HNC (3–2) ($\nu_{\text{rest}} = 271.98$ GHz) in band 6. The channel width was 122 kHz for band 3 and 244 kHz for band 6, corresponding to velocity resolution of 320 m/s and 270 m/s respectively. The total bandwidth is 468 MHz for band 3 and

Table 1. Details of ALMA observations taken between 2015 – 2016 in Cycle 3 observation campaign under the project 2015.1.00483.S. See Sec. 2.2 for further details.

	Band 3		Band 6	
Date	2015 Dec 26, 2016 Jan 13	2016 May 26	2016 Jan 10, August 16	2016 Jan 15, 16
Number of antennas	34 (main array), 11 (ACA)	34	44	46
Baseline length (m)	15 – 310, 8 – 43	15 – 640	15 – 1500	15 – 331
Primary beam (")	53, 91	55	23	23
Synthesized beam (")	$2.62 \times 2.06, 15.96 \times 8.49$	1.4×1.3	0.68×0.62	1.25×0.97
Line rest frequency (GHz)	115.27 (CO v=0, 1-0)	110.20 (13CO v=0 1-0)	265.88 (HCN v=0 J=3-2)	271.98
Spectral resolution	122 kHz (320 m/s)	122 kHz (332 m/s)	244 kHz (275 m/s)	244 kHz (269 m/s)
Calibrators (Amplitude, bandpass, phase)	Ganymede/Mars, J1427-4206 J1321-4342/J1352-4412	Ganymede J1427-4206, J1321-4342	Ganymede J1427-4206, J1352-4412	Callisto J1427-4206, J1352-4412

Table 2. CO luminosity from four regions named in the first column and shown in Fig. 5. Second column displays the array used, third column – measured integral flux density S_{CO} , and the last column – the line luminosity L_{CO} using the standard conversion (Solomon et al. 1997).

Region	Array	S_{CO} [Jy km s $^{-1}$]	L_{CO} [erg s $^{-1}$]
Reg1	12-m Main	3.0×10^4	1.997×10^{38}
Reg2	12-m Main	5.78×10^4	3.848×10^{38}
Reg3	12-m Main	6.9×10^4	4.593×10^{38}
Reg4	7-m ACA	7.3×10^5	4.86×10^{39}

937 MHz in band 6. The details of individual observations can be found in Tab. 1.

The Common Astronomy Software Application (CASA v4.7.2, McMullin et al. 2007) was used to perform calibration and imaging. Standard calibrations were performed for atmosphere, water vapor radiometer phase corrections, bandpass, amplitude and phase calibrations following the ALMA data reduction process. Cen A is a compact and strong continuum source that facilitates using self-calibration to improve the signal noise. We performed phase and amplitude self calibration using line-free channels and dedicated continuum spectral windows. After the calibrations, the executions for the same schedule block were combined together for imaging using the CLEAN algorithm with the CASA task `tclean`. The continuum source was imaged using line-free channels and continuum spectral windows using the multifrequency synthesis technique with the Briggs weighting and robust parameter +2.0 (natural weighting). The continuum emission was subtracted using the task `UVCONTSUB` using a linear fit to the line-free channels. The resulting continuum-subtracted data were then imaged with `tclean` with Briggs weighting with the same robust parameter of +2.0 to create a spectral cube. The rms noise per channel is ~ 10 mJy. The achieved synthesized beam (angular resolution) is $2.62'' \times 2.06''$ and $1.4'' \times 1.3''$ for band 3 main array observations, $15.96'' \times 8.49''$ for the ACA, and $0.68'' \times 0.62''$ & $1.25'' \times 0.9''$ for the band 6 data. Final images, Figs. from 1 to 5, were created using Astropy (Astropy Collaboration et al. 2013) and are discussed in Sec. 2.4 below.

2.3 Chandra X-ray data

X-ray images are needed to follow the distribution of the hot matter which may be located co-spatially with cold molecular gas. The

overlapping ALMA and *Chandra* emission is a starting point in our research. Therefore, in the next step, we retrieved and analyzed a deep (~ 110 ksec) *Chandra* observation of Cen A (ObsID 20794, PI: P. Nulsen, see also Snios et al. 2019) performed on September 19 2017. The observation was taken in FAINT mode, with the core placed at the aimpoint of the ACIS-S3 chip. The data were reprocessed using the `chandra_repro` script of the *Chandra* Interactive Analysis of Observation (CIAO) software (v. 11) with the calibration files CALDB version 4.8.2 (Fruscione et al. 2006). After filtering for background flares with the CIAO task `deflare`, the exposure time was ~ 107 ksec.

An exposure-corrected image of the central region was created with the `fluximage` script. The image is in the 0.5–7 keV energy band (with an effective energy of 2.3 keV) and binned to 1/4 of the native ACIS pixel size (0.123 arcsec/pix). The final image of the X-ray map from the innermost region of Cen A combined with ALMA emissivity contours, is presented in Figs. 1 and 3, and discussed in Sec. 2.4 below.

2.4 Coexistence of the hot and cold phase in Cen A

Fig. 1 shows the *Chandra* X-ray extended emission (given by the colour map) with the ALMA CO line integrated flux (shown by the contours). The X-ray colour map displays emission from the AGN, the diffuse emission of the inner jet, hot gas in the central region, and point-like sources corresponding to jet knots and field sources. The hole visible at the centre of the AGN emission and the streak crossing the image in the north-west to south-east direction are artifacts (pile-up and read-out streak, respectively) caused by the brightness of the AGN. The bottom image in Fig. 1 zooms in on the diffuse X-ray emission, which extends up to $5''$ ($= 92$ pc, 2.8×10^{20} cm) from the centre. The integrated CO (1 – 0) line flux shows the circumnuclear disk which surrounds the inner hot X-ray emission. The region of integration is given in Fig. 5 by the red circle and named Reg1.

The CO (1 – 0) line emission from Cen A is shown in Fig. 2, where the top image shows the integrated flux density map from the ALMA compact array (ACA), the middle image shows the integrated flux density map from the ALMA main array, and the bottom image gives the velocity map. The contours are the CO (1 – 0) integrated flux density from the ALMA main array. In Fig. 3, the ^{13}CO (1 – 0), C^{18}O (1 – 0), CS (2 – 1) and CO (1 – 0) molecular lines integrated flux density contours are overlaid on the X-ray colour map. Fig. 4 shows the integrated flux density maps for the HCN (3 – 2), HCO^+ (3 – 2) and HNC (3 – 2) molecular lines ob-

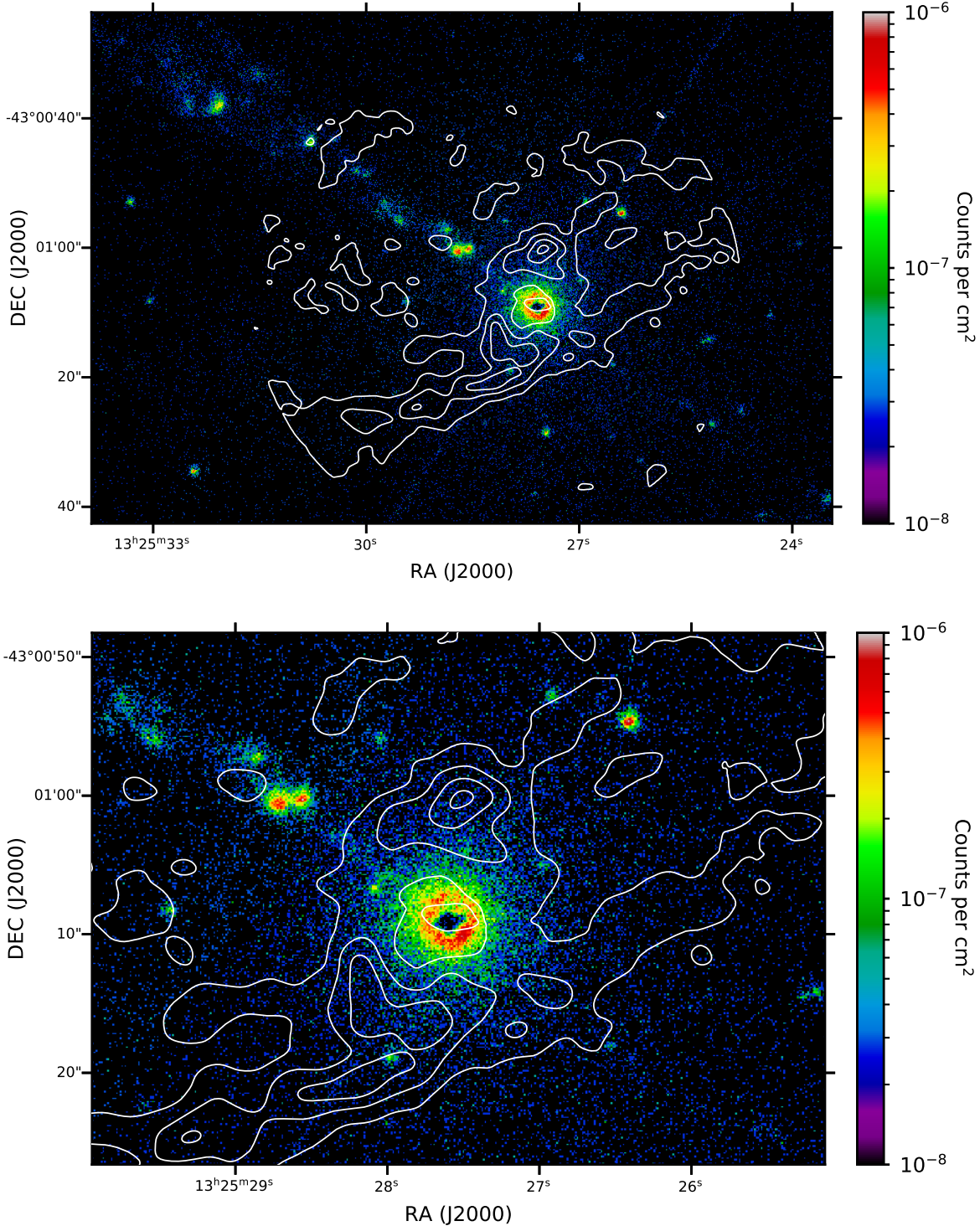


Figure 1. *Chandra* X-ray images together with ALMA contours. The top image shows the central 1 kpc of Cen A in X-ray, with overlaid integrated CO (1 – 0) flux density contours from ALMA. The contour levels are (4, 7.66, 11.33, 15) Jy beam^{–1} kms^{–1}. The bottom image shows the central 200 pc region of interest for this work.

served in the band 6 of ALMA main array, with the CO (1 – 0) line contours overlaid.

The ALMA data allow us to detect line luminosities from the very central region which overlaps with *Chandra* data. Since the most prominent is CO (1 – 0) line emission, we present the ob-

served luminosity of this line in Tab. 3 for different regions. Beside the standard luminosity taken from the central region named Reg1, we have extracted the luminosities from neighbouring more luminous regions marked in Fig. 5 as Reg2 and Reg3, and from the most luminous region observed in the total field of view marked

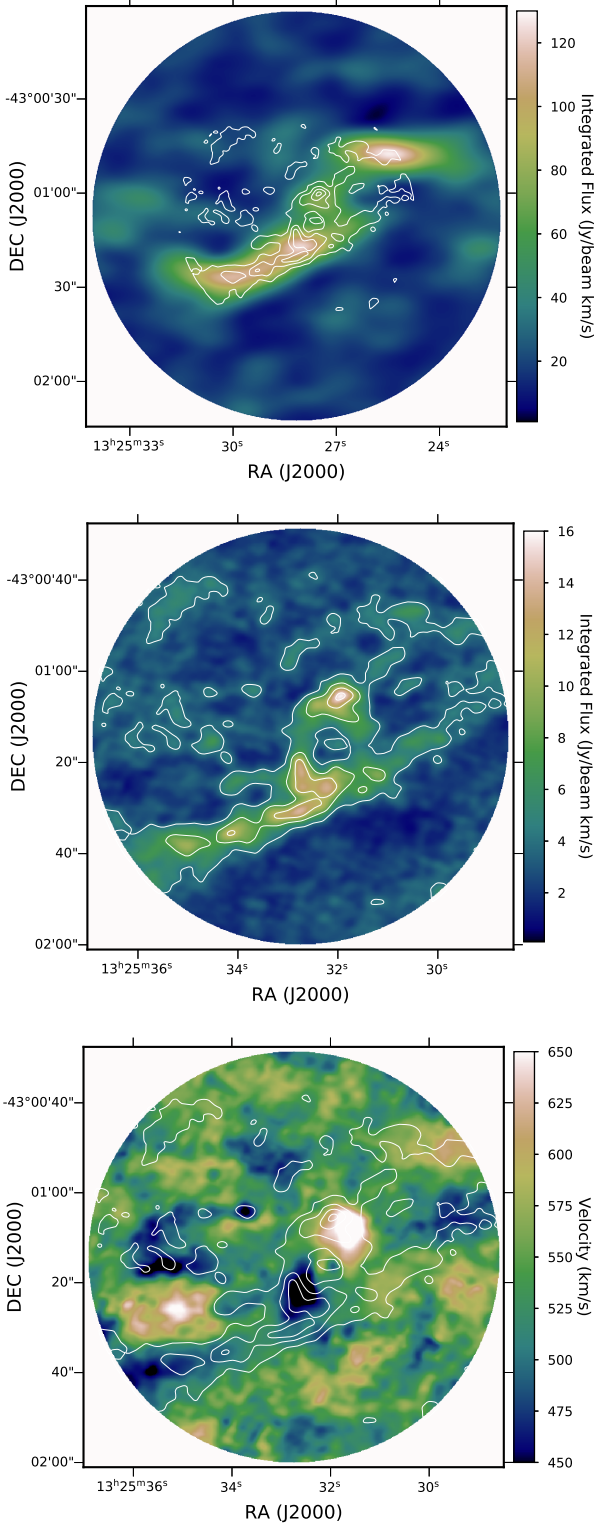


Figure 2. Cen A in CO (1 – 0) line - 115.271202 GHz. Top - 7 m ACA. MIDDLE - ALMA main array, contours show the CO (1 – 0) emission with ALMA main array (same as fig. 1). Bottom - velocity map (V_{LSR} for Cen A $\sim 547 \text{ km s}^{-1}$).

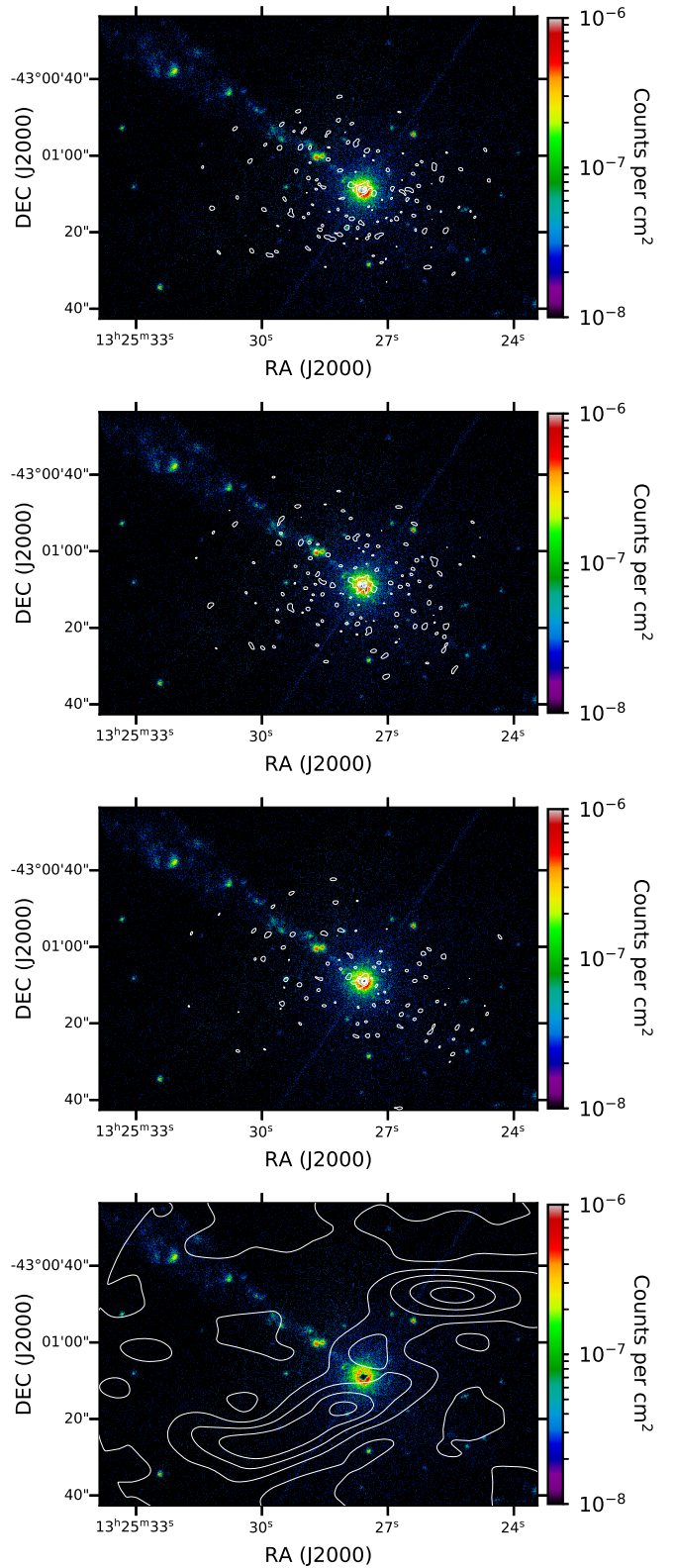


Figure 3. Cen A in four molecular lines: top ^{13}CO (1 – 0) - 110.201354 GHz, middle/top - C^{18}O (1 – 0) - 109.782176 GHz, middle/bottom - CS (2 – 1) - 97.980953 GHz, and bottom - CO (1 – 0) from 7 m ACA. Contours show the integrated flux densities of the lines mentioned, overlaid on the *Chandra* image. Contour levels are: top: (1.3, 2.5, 3.7, 4.9, 6.1), middle two: (1.2, 2.275, 3.35, 4.425, 5.5), bottom: (15, 40, 65, 90, 115) $\text{Jy beam}^{-1} \text{ km s}^{-1}$.

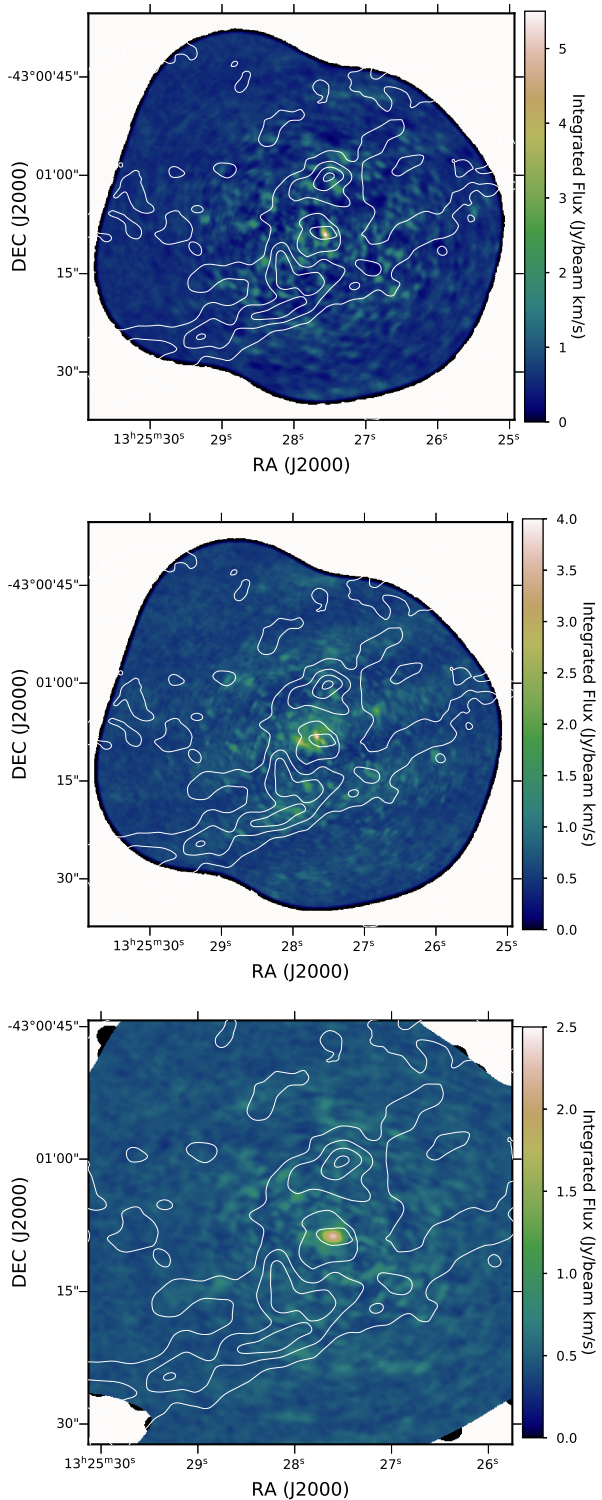


Figure 4. Cen A in three lines: top - HCN (3 – 2) - 265.886431 GHz, middle - HCO+ (3 – 2) - 267.557633 GHz, bottom - HNC (3 – 2) - 271.981111 GHz. Contours indicate CO (1 – 0) emission (same as fig. 1).

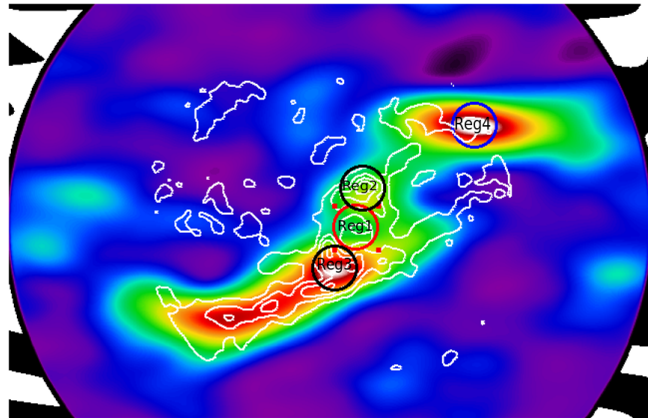


Figure 5. Regions marked in the map for which, the CO luminosity was calculated. Reg1 is the central region, while Reg2 and Reg3 are regions of the same size taken by the 12-m ALMA Main array. The most luminous region of the same size is detected by 7-m ACA, and marked as Reg4.

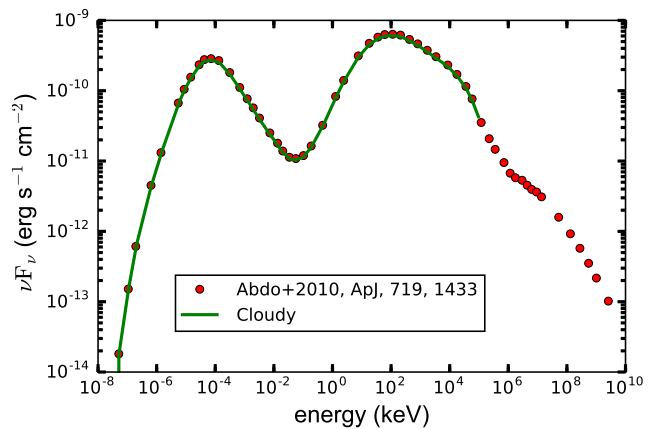


Figure 6. Spectral energy distribution (SED) of the Cen A nucleus from multi-wavelength observations given by points. The solid curve presents SED used in this paper for photoionization calculations with the CLOUDY code.

as Reg4. The calculation was done using the standard formula (for details see: [Solomon et al. 1997](#)) of extracting line luminosity L_{CO} in erg s^{-1} , from observed integrated flux density S_{CO} in Jy km s^{-1} detected by ALMA and given in the third column of Tab. 3.

2.5 Spectral Energy Distribution

The spectral energy distribution of radiation which illuminates the nuclear gas in the vicinity of the SMBH is a crucial parameter in photoionization calculations. Thus it is important to use appropriate SED of Cen A responsible for the TI mechanism operating in the source. In the case of Cen A, with a prominent jet, we investigate the impact of a jet dominated radiation field on multi-phase medium. The most adequate SED from the central region of Cen A was published by [Abdo et al. \(2010\)](#), presented in Fig. 6, with data from different instruments, including VLBI, *Swift*, *XMM-Newton*, *Suzaku*, *Fermi*-LAT, and HESS, and were observed in dif-

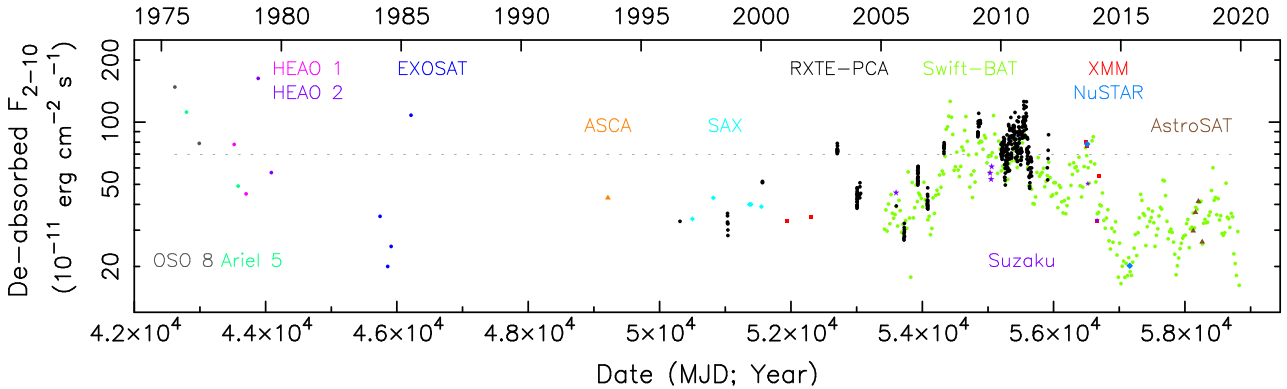


Figure 7. Historical unabsorbed 2 – 10 keV power-law flux; references are listed in Section 2.1. The dashed line is the long-term mean, 7.9×10^{-10} erg cm $^{-2}$ s $^{-1}$, which for a luminosity distance of 3.8 Mpc, corresponds to a 2–10 keV luminosity of 1.4×10^{42} erg s $^{-1}$.

ferent epochs. Below we discuss the reliability of this SED due to the variability of the source and the enormous impact of the jet.

Cen A is a variable source in the keV/MeV energy range. Locally-measured spectral slopes in the keV/MeV range seem relatively constant over time, despite large flux variations. The photon power-law index Γ is usually ~ 1.8 from $\lesssim 1$ keV (where there is continuum absorption along our line of sight) up to ~ 150 – 200 keV (e.g. Jourdain et al. 1993; Kinzer et al. 1995; Rothschild et al. 2006). The measured intrinsic neutral hydrogen absorption is usually $N_{\mathrm{H}} \sim 1$ – 2×10^{23} cm $^{-2}$. Above $\gtrsim 150$ keV, the spectrum steepens to ~ 1.9 – 2.3 (Kinzer et al. 1995), modeled a power-law with a sharp break here, but the rollover is likely gradual). That $\Gamma = 2.3$ portion extends up to very roughly 10 MeV, above which Γ might steepen again slightly (Fig. 3 of Steinle et al. 1998). The γ -ray emission in the 100 MeV to 3 GeV energy range is well-reproduced by a power-law with $\Gamma = 2.70$. Above 3 GeV, flattening of the spectrum is observed, with $\Gamma \sim 2.3$ until roughly 100 GeV, which could be indicative of an emerging additional component. Above ~ 100 GeV, Γ steepens to 2.52 continuing into the 0.3 – 10 TeV range (H. E. S. S. Collaboration et al. 2018, see their Figs. 1 and 3). A monitoring of the flux over time was carried out in the X-ray window. At higher energies, due to the lower count statistic, good signal-to-noise spectra were obtained by binning over long (month-to-years) time intervals. However, MeV-GeV spectra are roughly consistent between the CGRO (early 1990s) and Fermi (2008–2016) eras.

The SED constructed by Abdo et al. (2010) has the typical double-hump shape of non-thermal, jet related emission. In the framework of leptonic models, the low energy curve is synchrotron emission, while the high-energy curve is usually ascribed to Compton scattering of different seed photons. For example in Abdo et al. (2010), two models were considered to explain the origin of the high-energy component. In the first model, the X-ray to gamma-ray band is produced via upscattering of the synchrotron photons by the electrons in the jet (synchrotron self Compton, SSC). In the second scenario, the emission was produced by upscattering of the synchrotron photons produced in a fast-moving spine by the electrons in a slow moving layer. Most relevant for the purpose of this work is that, depending on the bulk motion of the emitting region and the jet axis inclination with respect to the observer viewing angle, the intrinsic emission can be boosted or deboosted in the observer’s rest frame.

Taking all above into account, we decided to omit the most energetic part of the spectrum (above 10⁵ keV), which can originate

from the boosted jet, and may not affect the close environment of the SMBH. The full shape of the spectrum used in our numerical calculations is presented in Fig. 6 by a solid line, and discussed in Sec. 3. Since we can expect that the beaming factor may differ, and since the observed flux depends on the beaming factor with the power of fourth, we should take into account that the overall luminosity which affects the cold gas may change by a factor of several and we take it into account in our computations (see Sec. 3.1 for details).

2.6 Extracting the Cen A bolometric luminosity

The bolometric luminosity of the radiation intercepting the nuclear gas is the second important input parameter for our photoionization calculations. In case of Cen A, which is a variable source dominated by jet emission, the estimation of such luminosity is challenging. On one side, we can compute the bolometric luminosity from the integration of the broad band observations presented in Fig. 6, which gives $L_{\mathrm{bol}} = 9.45 \times 10^{42}$ erg s $^{-1}$. On the other side, the innermost hot plasma accreting on the SMBH can also be the source of radiation affecting the molecular gas. Therefore, the estimation of the X-ray luminosity of the hot gas from the range between 2 – 10 keV, which directly illuminates the cold gas may be crucial to achieve proper value for Cen A.

From observations, the 2 – 10 keV X-ray luminosity lies in the range 5 – 9×10^{41} erg s $^{-1}$ (Evans & Koratkar 2004; Rothschild et al. 2011). Assuming the X-ray bolometric correction factor of $10^{1.4}$ (Duras et al. 2020), the bolometric luminosity from X-ray data is: $L_{\mathrm{bol}} = 0.3$ – 2×10^{43} erg s $^{-1}$. These values are compatible with the value of the bolometric luminosity obtained by integrating the SED over solid green line marked in Fig. 6.

We show in Fig. 7 a historical lightcurve of unabsorbed 2 – 10 keV flux spanning 44 years to follow the variability in the luminosity of Cen A. Non-RXTE data from 2000 and earlier were taken from Risaliti et al. (2002, see individual references therein). We obtained Swift-BAT data from the Swift/BAT Hard X-ray Transient Monitor website² and rebinned them to 20 days, and extrapolated from the 15 – 50 keV count rates (hereafter CR_{15–50} in units of cts cm $^{-2}$ s $^{-1}$), to estimate unabsorbed 2 – 10 keV power-law fluxes. Based on the 70-month average BAT spectrum of Cen A, we assumed a power-law photon index of 1.87, and a conversion of F_{2-10}

² <https://swift.gsfc.nasa.gov/results/transients/>

$(10^{-11} \text{ erg cm}^{-2} \text{ s}^{-1}) = 5726 \text{ CR}_{15-50}$. Reduction of *Suzaku* XIS and HXD data followed standard extraction procedures, and using spectral models based on [Markowitz et al. \(2007\)](#) and [Fukazawa et al. \(2011\)](#). The 2013 Nuclear Spectroscopic Telescope ARray (*NuSTAR*) flux was estimated from the best-fit spectrum of [Fürst et al. \(2016\)](#). Reduction and fitting of the 2015 *NuSTAR* data followed e.g., [Fürst et al. \(2016\)](#) and will be detailed in a future paper by Markowitz et al., (in prep.). Reduction and fitting of *XMM-Newton* EPIC PN data followed e.g., ([Evans & Koratkar 2004](#)). Reduction and fitting of *RXTE*-PCA data followed standard procedures, e.g., ([Rivers et al. 2011](#)). Reduction and fitting of *AstroSAT* SXT and LAXPC data will be detailed in a future paper (Markowitz et al., in prep.). Assuming a luminosity distance of $3.8 \text{ Mpc} = 1.2 \times 10^{25} \text{ cm}$ ([Rejkuba 2004](#)), this flux yields an (assumed isotropic) $2 - 10 \text{ keV}$ luminosity of $1.1 \times 10^{42} \text{ erg s}^{-1}$ (including BAT; $1.2 \times 10^{42} \text{ erg s}^{-1}$ excluding BAT). Fig. 7 clearly demonstrates that the X-ray flux can change by a factor of roughly 10 over timescales of \sim a decade.

To derive a robust AGN X-ray luminosity for Cen A ($2 - 10 \text{ keV}$ band), we used the *NuSTAR* observations ([Harrison et al. 2013](#)). Though *NuSTAR* encompasses the $3 - 78 \text{ keV}$ energy band and has a broader point spread function (PSF) than *Chandra* with half-power diameter of 60 arcsec ([Madsen et al., 2015](#)), the instrument uses triggered readout to log detected photon events that eliminates pile-up. The nearest *NuSTAR* observation in time to the *Chandra* observation analysed here is ObsID 60466005002, performed on 23 April 2018. We produced calibrated and cleaned events files and extracted spectra from 100 arcsec circular regions for each focal plane module (FPM). We then extracted background spectra from a circular region as large as possible on the same detector chip as the source per FPM.

To estimate the Centaurus A AGN flux and luminosity we fit the *NuSTAR* spectrum extracted for the AGN, with each FPM spectrum binned to a minimum of 25 counts per bin. Our model is an absorbed power-law and Gaussian Fe $K\alpha$ emission line. This gives $\chi^2/n = 1344.88/1381$, where n the degrees of freedom. The total observed flux for this model is $F_{2-10\text{keV}} = 2.4 \times 10^{-10} \text{ erg s}^{-1} \text{ cm}^{-2}$ in both FPMA and FPMB. At the distance of Centaurus A ($D = 3.8 \text{ Mpc}$), this gives an observed (i.e. absorbed) luminosity of $\log L_{2-10\text{keV}} / \text{erg s}^{-1} = 41.6$ for the AGN. This corresponds to an unabsorbed luminosity of $\log L_{2-10\text{keV}} / \text{erg s}^{-1} = 41.9$ for the AGN in both FPMA and FPMB.

To test the contribution of contaminants in the *NuSTAR* spectrum, we manually extracted off-nuclear sources of flux in the *Chandra* events file for Centaurus A. A total of 10 off-nuclear point-source contaminants and both the jet and counter jet components were clearly visible with *Chandra* located inside the extraction region used for the *NuSTAR* source spectrum. By fitting each contaminant separately, and summing the predicted $2 - 10 \text{ keV}$ flux, we find that the observed $2 - 10 \text{ keV}$ flux for the AGN is a factor of ~ 50 times higher than the combined flux from the 12 total contaminants manually extracted, further indicating that we are estimating the AGN flux robustly with *NuSTAR*.

This gives a $2 - 10 \text{ keV}$ luminosity of $L_X = 3.98 \times 10^{42} \text{ erg s}^{-1}$ for the AGN in Cen A. Taking into account the bolometric correction factor, $L_{\text{bol}} = 1 \times 10^{44} \text{ erg s}^{-1}$, at the date closest to the *Chandra* observations. Assuming that only ten percent of this emission originates from the inner hot radius, while the rest comes from the jet, we take $L_{\text{bol}} = 1 \times 10^{43} \text{ erg s}^{-1}$ as a reference value for our calculations.

After considering the information on the uncertainty of the jet beaming factor, the variability of X-ray flux, and the bolometric luminosity estimation, we followed our first paper [Różańska et al.](#)

(2014) where several luminosity states for Sgr A* were considered in photoionization calculations. In the case of Cen A studied here, we consider two luminosity states, differing by a factor of 70, and keeping the same overall SED shape as given in Fig. 6. When Cen A has normal high luminosity state we assume our reference value of $L_{\text{bol}} = 1 \times 10^{43} \text{ erg s}^{-1}$, while for the low luminosity state we take $L_{\text{bol}} = 1.43 \times 10^{41} \text{ erg s}^{-1}$. All important properties of the Cen A inner region used for our simulations are listed in Sec. 3.1.

3 SET-UP OF THE MODEL

To model multi-phase gas in the centre of Cen A, we use the same approach as in our previous work dedicated to Sgr A* ([Różańska et al. 2014](#)) and M60-UCD1 ([Różańska et al. 2017](#)). Multi-phase environment can form spontaneously by the irradiation-induced effects of TI ([Field 1965](#)). It operates only for a certain range of parameters (e.g., [Cox 2005](#), and further references therein), but the most important is the occurrence of strong ionization, which means that (I) interstellar medium (ISM) gas should be metal rich ([Hess et al. 1997](#)), and (II) an illumination field should be hard enough to be able to remove all electrons even from heavy atoms, and display substantial luminosity. Such radiation is often observed from the central accreting SMBH, and can provide to the multi-phase medium in the close vicinity of SMBH ([Krolik et al. 1981; Różańska & Czerny 1996](#)). Hence, the shape of irradiated photons and its luminosity are crucial parameters of our study.

Other essential parameters of our modeling are connected to the gas properties which include the distance of the considered region from the source of radiation, gas density, its total column density and eventual dust abundance. This is implemented with the CLOUDY 17.01 ([Ferland et al. 2017](#)) photoionization code, which computes a transfer of radiation through matter with different geometries, allowing to choose ISM abundance with dust. All important radiative processes which heat or cool plasma are taken into account, such as free-free emission, atomic bound-free processes, and bound-bound transitions between different ion states.

The radiation field may originate from the extended inner part of the jet, nuclear star cluster (NSC) stars or from the hot plasma around the SMBH. In our previous work concerning Sgr A* and M60-UCD1 ([Różańska et al. 2017](#)), we have taken into account additional radiation field from the NSC, but in the case of Cen A, the starburst activity is negligible compared to the emission from the AGN ([Radomski et al. 2008](#)). Therefore, for the purpose of this paper we neglect any additional energy input by photons from stars.

Further complications may arise when the region under consideration is dominated by mechanical energy input from stellar winds or outflows ([Quataert 2004; Silich et al. 2004, 2008](#)). This was accounted for the case of Sgr A* and M60-UCD1, where such energy input by winds was reported (see discussion in [Różańska et al. 2017](#)). Nevertheless, in the case of Cen A it has been reported that close to the SMBH, the X-ray dominated region (XDR) dominates over mechanical heating ([Fürst et al. 2016; Espada et al. 2017](#)). Under these circumstances, we neglect mechanical energy input in our computations. For the full treatment of the multi-phase media hydrodynamic simulations with radiation should be made (see [Waters & Proga 2019; Dannen et al. 2020](#), and references therein), but those simulations still do not consider many atomic processes i.e. lines and cannot be directly compared with data.

Depending on the profile of the spectral energy distribution (SED), the incident radiation field can both cool and heat the plasma. The net effect is determined by plasma density as well as

the spectral shape of the incident radiation. Thus, the presence of the radiation field contributes both to the cooling and heating rates, i.e., \mathcal{L} and \mathcal{H} , respectively in $\text{erg s}^{-1} \text{cm}^{-3}$. The difference between these two parameters describes the rate of exchange of total energy per unit volume by different cooling and heating processes.

Recent studies (Różańska et al. 2006; Baskin et al. 2014; Adhikari et al. 2015, 2018; Adhikari 2019; Adhikari et al. 2019) have demonstrated that the gas clouds illuminated by the radiation field in various astrophysical environment remain in total (radiation + gas) pressure equilibrium as it is dominated by the radiation pressure. We refer the reader to Adhikari et al. (2018) and Adhikari (2019) for the relevant discussion on the validity and differences between the constant pressure and constant density assumptions used in the photoionization modelling. Following this, we adopt the assumption of constant pressure in all the model commutations presented in this paper.

To solve for the stability of thermal equilibrium, we employ CLOUDY 17.01 (Ferland et al. 2017). This solution provides us with the local equilibrium temperature of the medium as a function of assumed ISM hydrogen density at a given location. The stability can be conveniently estimated from the diagram of stability curve. The definition of the ionization parameter Ξ (Tarter et al. 1969) is,

$$\Xi = \frac{L}{4\pi c P_{\text{gas}} R^2}, \quad (1)$$

where L is the source luminosity, P_{gas} is the local gas pressure, and R is the distance from the centre. The curve Ξ vs. T indicates the thermal stability. In this relation, the branch with the positive slope is radiatively stable while the branch with the negative slope is unstable.

The equation above requires the knowledge of additional parameters, in order to construct a full photoionization model. Besides the SED and bolometric luminosity, we have to assume the density of the matter at the illuminated cloud surface, n_{H} , the location of the matter from the nucleus R , and the total column density of the nuclear gas N_{H} . While the value of both densities is not precisely known, the location of cold and hot material can be adopted from the high resolution images presented in previous section.

3.1 Model parameters for Cen A

For the purpose of this paper we adopt the averaged value of $M_{\text{BH}} = 6 \times 10^7 M_{\odot}$. For such mass the gravitational radius is $R_g = 8.12 \times 10^{12} \text{ cm}$, and $R_{\text{Schw}} = 1.62 \times 10^{13} \text{ cm}$. We assume a cloud at a certain distance from the nucleus with abundant with heavy elements as typical for Solar abundances. Alternatively, we also consider a cloud consisting of a mixture of gas and dust in the proportions appropriate for the ISM (standard option in CLOUDY).

For all cases, we consider the shape of the illuminated SED as presented in Fig. 6 by the green solid line. To account for X-ray spectral variability, uncertainty of the jet beaming factor, and of the bolometric luminosity estimation, we consider two luminosity states discussed in Sec. 2.1 with the same spectral shape. When Cen A is in the high luminosity state we assume $L_{\text{bol}} = 1 \times 10^{43} \text{ erg s}^{-1}$, and for the low luminosity state we take $L_{\text{bol}} = 1.43 \times 10^{41} \text{ erg s}^{-1}$.

The most uncertain parameter in the CLOUDY calculations is the gas density. We assume hot plasma filling the space with density $n(r) = n_0 * (r/r_0)^{-1.5}$. From older *Chandra* observations, Kraft et al. (2003) estimated the density $n_0 = 3.7 \times 10^{-2} \text{ cm}^{-3}$, and $r_0 = 10 \text{ pc}$, which we use for our reference model of a single cloud with density $n_{\text{H}_0} = 3.7 \times 10^{-2} \text{ cm}^{-3}$ at the cloud surface, located at 10 pc from

the nucleus and illuminated by the high luminosity state. We also use additional values of density to test the dependence of results on density (sec. 4). We assume that each cloud is under constant pressure, and thus the value of density is defined only at the illuminated cloud surface. Under this assumption, the density and ionization structure is stratified deep inside the cloud if enough column of matter is considered.

We construct the stability curve using CLOUDY simulations to test the stability of gas clouds. We conducted stability analysis in two ways. (I) To reconstruct the stability curve at a certain radius, we adopt geometrically thin clouds in the range of densities from $\log(n_{\text{H}_0} [\text{cm}^{-3}]) = -3$ to 13. (II) Secondly, the low density, geometrically thick single cloud illuminated by the incident SED can be used to reconstruct the stability curve. Such a cloud, being under constant pressure, becomes strongly stratified due to irradiation.

When constructing the stability curve for thin clouds of different densities, we perform photoionization calculations for three distinct distances from the nucleus at which the clouds are located. In other words, we construct three stability curves at distances: $R = 5.69 \times 10^{20} \text{ cm}$ (10'', 184.25 pc, $\log(R) = 20.755$), $R = 2.85 \times 10^{20} \text{ cm}$ (3'', 55 pc, $\log(R) = 20.230$), and $R = 3.50 \times 10^{19} \text{ cm}$ (0.62'', 11.5 pc, $\log(R) = 19.544$). The last value is the best spatial resolution of ALMA in our observations. The location of the single low density, geometrically thick cloud used in the photoionization modeling depends on the location of the hot illuminated cloud surface, and signifies how far from the nucleus cold matter is extended. We place the illuminated cloud surface at three distances: $R = 1.54 \times 10^{20} \text{ cm}$ (2.71'', 50 pc, $\log(R) = 20.187$), $R = 6.16 \times 10^{19} \text{ cm}$ (1.09'', 20 pc, $\log(R) = 19.789$), and $R = 3.08 \times 10^{19} \text{ cm}$ (0.54'', 10 pc, $\log(R) = 19.488$). The smallest 10 pc radius is not resolved in the X-ray observations, but it is used to calculate the temperature of the inner plasma. All the distances are still significantly larger than the gravitational radius.

4 RESULTS

The stability curves for three different distances from the centre and for two different chemical abundances are presented in the Fig. 8. The upper panels of the figure display the curves computed for the ISM abundances with dust (blue points) and without dust (red points) while the lower panels display the curves for Solar composition with dust (black points) and without dust (green points). Each point represents a thin cloud under constant pressure and illuminated by the same radiation field of the Cen A SED and reference value of L_{bol} . As the ionization parameter $\Xi = P_{\text{rad}}/P_{\text{gas}}$, vertical lines on the stability curves indicate clouds under constant pressure. Figure 8 shows that hot gas with temperature of the order of 10^8 K emitting in X-rays can coexist with cold matter at $\sim 10^4 \text{ K}$ emitting in visible light. Nevertheless, dusty clouds do not coexist with hot X-ray plasma, and can only coexist with cold gas, due to evaporation from X-rays. Note that changing the ISM composition to Solar only slightly influences the shape of the stability curve and only in cold dusty regions. Since cold regions are most probably composed of interstellar matter, we accept ISM composition for further considerations.

Next, we computed various model structures for geometrically thick dusty clouds, located at the representative distances of 10, 20 and 50 pc, and for relatively large column densities from $N_{\text{H}} = 1 \times 10^{23}$ up to $1 \times 10^{24} \text{ cm}^{-2}$. The large values of N_{H} ensure that the radiation passes across the depth of cloud and reaches the minimum temperature at which the molecular emission is sig-

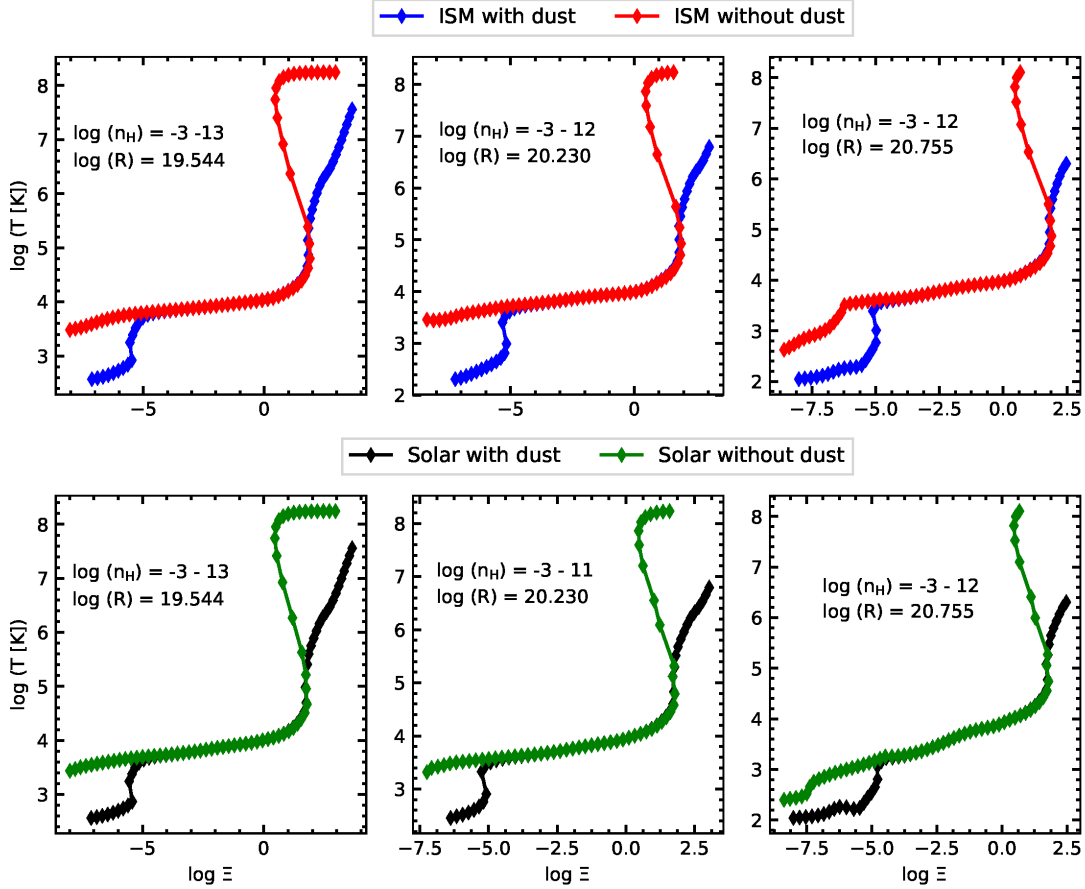


Figure 8. Stability curves for two different heavy element abundances: upper panels - ISM abundances, bottom panels - Solar abundances, and increasing radii, left to right. Each panel contains calculations with and without dust. Each point in the curve represents the model computed for one starting density. The range of computed densities is given at each panel. The SED luminosity is always kept at $L_{\text{bol}} = 1 \times 10^{43} \text{ erg s}^{-1}$.

nificant. The temperature, density structures and stability curves for radii 10, 20, 50 pc are presented in Figs. 9, 10, and 11 respectively. These clouds are computed for an open thick geometry, with the assumption of constant pressure, and for the hydrogen number densities at the surface of the cloud: $n_{\text{H}_0} = 3.7 \times 10^{-4} \text{ cm}^{-3}$ – upper panels, $n_{\text{H}_0} = 3.7 \times 10^{-2} \text{ cm}^{-3}$ from Kraft et al. (2003) – middle panels, and $n_{\text{H}_0} = 3.7 \text{ cm}^{-3}$ – lower panels at three of the above figures.

The temperature profiles presented in the right panels of Figs: 9, 10, and 11 clearly indicate multi-phase medium. They display jumps at the instability zones. For the least dense cloud considered ($n_{\text{H}_0} = 3.7 \times 10^{-4} \text{ cm}^{-3}$), the material extends up to ~ 425 pc (23''), but in the case of the higher starting density ($n_{\text{H}_0} = 3.7$) the material extends only up to 20.34 pc (1.1''). The hot part indeed may be spherical, but changing the geometry in CLOUDY from open thick to closed i.e. spherical, does not change our results considerably. The CO line emission slightly decreases when the open geometry is replaced by the spherical geometry (see CLOUDY documentations for details).

We present the line luminosities from molecular lines that are observed with ALMA, which result from the computations of two individual clouds of different n_{H_0} in Tab. 3. The 13CO (1–0) line is not represented in our models. All other lines can be directly compared with observations, and the modelled lines roughly reproduce observational data.

4.1 Dependence on density

It is well known that there is a critical density for the thermal molecular emission i.e. density above which the particular line emission is visible at the certain luminosity (Loenen et al. 2007; Shirley 2015). The list of critical densities for the lines observed by ALMA in Cen A integrated over a circle of radius 4.5'', is given in Tab. 3 in the fourth column.

To study the density dependence, we searched the large parameter space with CLOUDY, using a single cloud under constant pressure for each set of input parameters, and see which clouds closely reproduce the molecular line luminosities deduced from ALMA data as presented in column 3 of Tab. 3. Figs 12 and 13 depict the model parameters: gas densities, column densities and radii used, and the resulting molecular emission obtained from CLOUDY models for the lines CO (1–0) and HCO^+ (3–2) respectively.

From Figs. 12 and 13, it is quite clear that the molecular line emission strongly depends on the value of the gas density used in the photoionisation models. The slight variation of line luminosities with the radial distance is also seen from both figures. In our case, enhanced molecular emission is obtained for the model with the lowest value of gas density considered at the illuminated face of the cloud i.e., $3.7 \times 10^{-4} \text{ cm}^{-3}$. This is due to the fact that the CO emission area in a low density cloud is much larger than in the case of a high density cloud. The difference between these two cases can

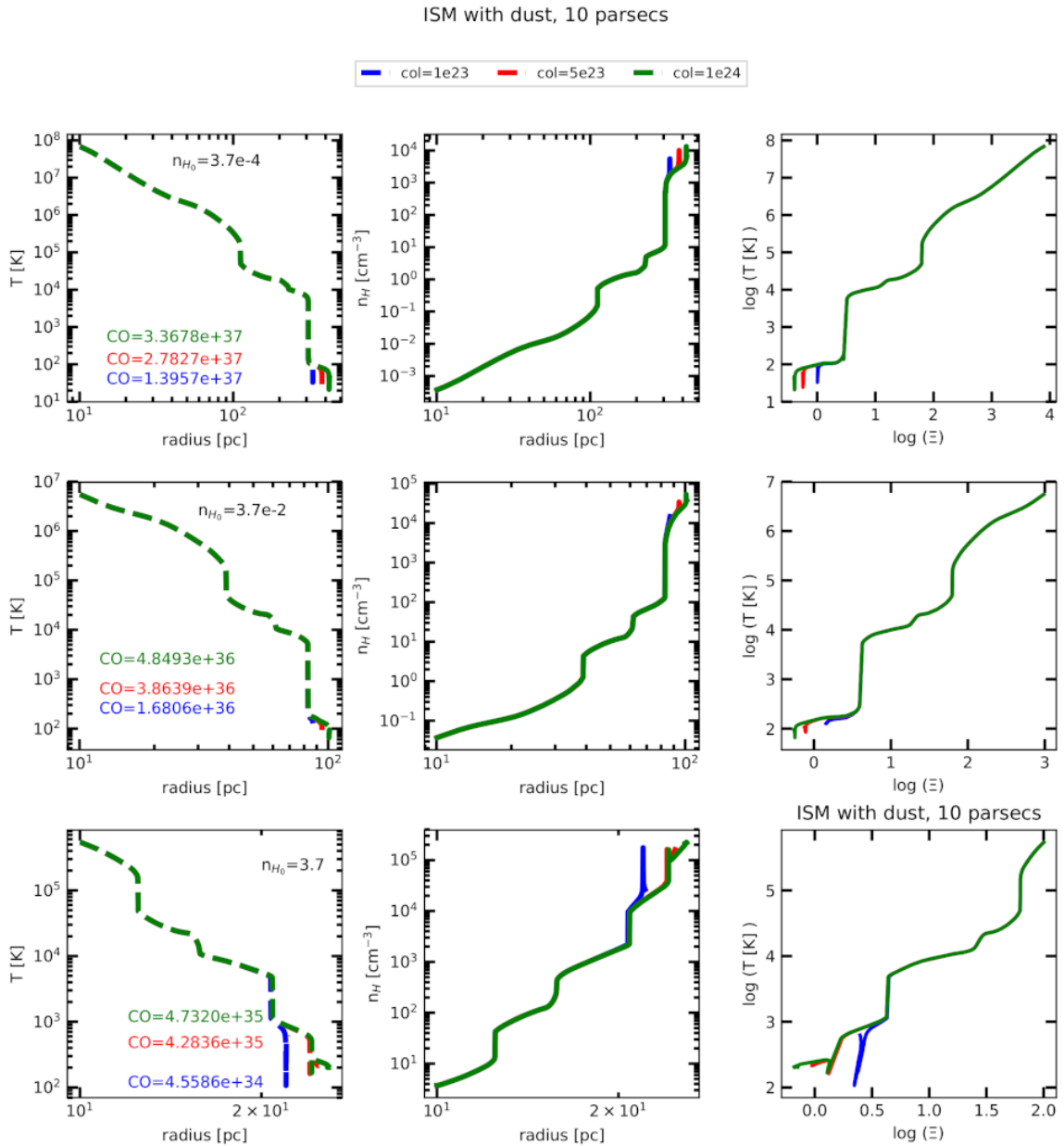


Figure 9. A single geometrically thick cloud structure for the location of illuminated cloud surface at 10 pc for three different starting densities: 3.7×10^{-4} cm^{-3} in the upper panels, 3.7×10^{-2} cm^{-3} (see Kraft et al. 2003) in the middle panels, and 3.7 cm^{-3} in the lower panels. From left to right the three columns represent: temperature radial structure in the left column, density radial structure in the middle column (plotted over the depth of the cloud in both columns), and the stability curves (plotted over the ionization parameter) in the rightmost column. The models are computed for the radiation luminosity of 10^{43} erg s^{-1} . Color of the solid lines indicates different total column density assumed in the computations, as shown on top of the figure; while color labels give the predicted CO (1 – 0) luminosities corresponding to the adopted column density.

be realized by comparing the first and third rows of Fig. 9. When the density increases by 4 orders of magnitude, the CO emission is reduced by 2 orders of magnitude. Note that, this reduction is directly related to the size of the emitting cloud before it reaches the backside of the cloud. The size of the CO emission cloud for the least dense cloud (3.7×10^{-4} cm^{-3}) is ~ 400 pc, whereas the size for the densest cloud (3.7 cm^{-3}) is ~ 28 pc (Fig. 9).

Fig. 14 shows the CO (1 – 0) luminosity as a function of the radial distance across the cloud. A comparison between the two

initial density cases; 3.7×10^{-4} and 3.7 cm^{-3} demonstrates that the CO emission comes from a large distance for the less dense gas. However, most of the emission is produced in the thin layer of the cloud as compared to its total size. This is due to the fact that CO (1 – 0) is produced in the low temperature region close to the backside of the illuminated cloud.

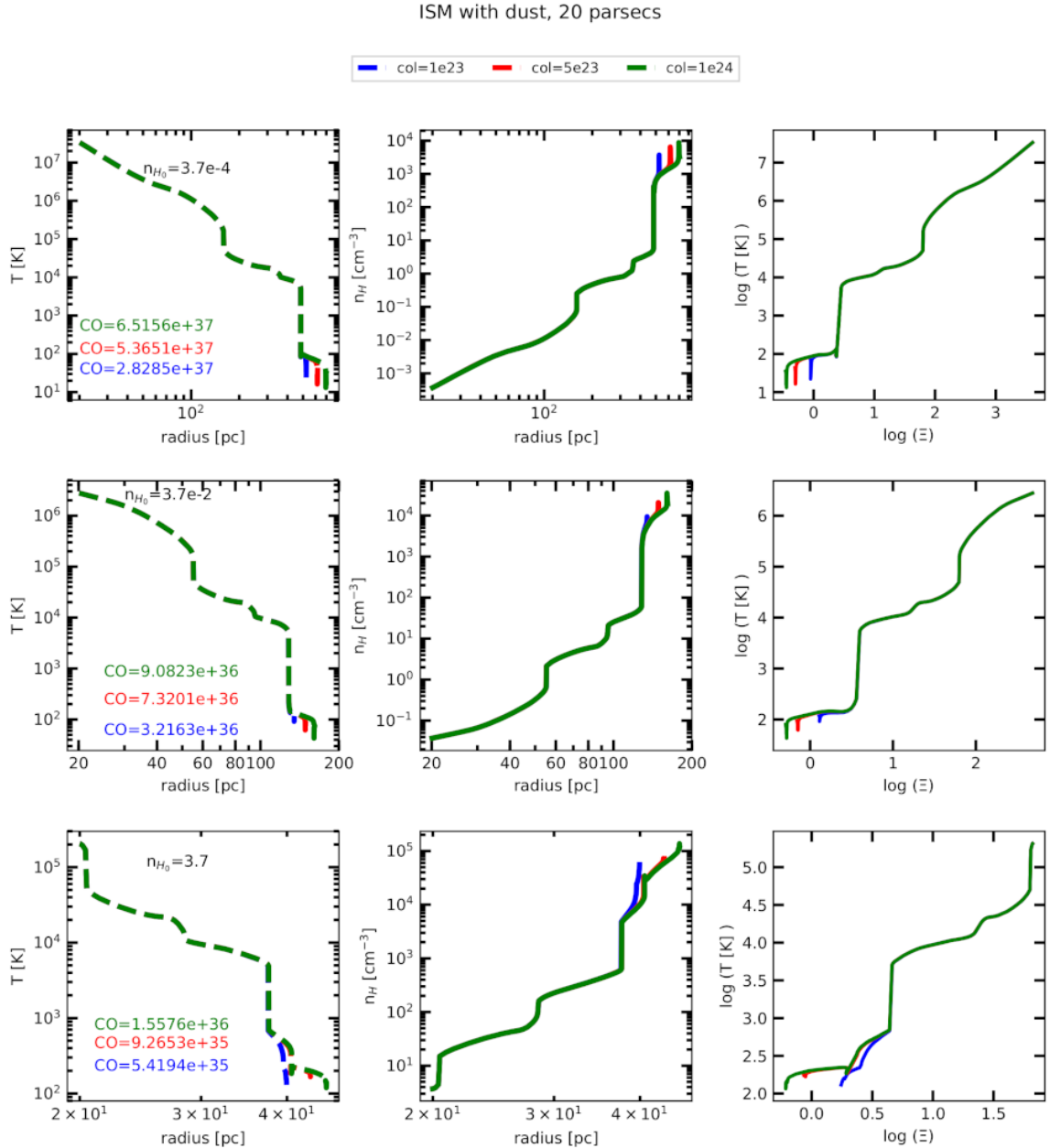


Figure 10. Same as in Fig. 9, but for an inner radius of 20 pc.

4.2 Dependence on the source luminosity

In order to study the effect of the luminosity on the molecular emission, we adopted the luminosity 1.43×10^{41} erg s $^{-1}$, which is lower by a factor of ~ 70 than the value considered previously, and we computed a CLOUDY single thick cloud model under the constant pressure condition at 10 pc radius. Only the source luminosity was changed while keeping the SED same as in Fig. 6. For such a low luminosity, the temperature, density and ionization structure computed for three different densities considered is shown in Fig. 15. Comparison between Figs. 9 and 15 demonstrates that the overall structure of the cloud does not differ significantly. However, the CO (1 – 0) luminosity is an order of magnitude lower for low density cloud for the low luminosity case (upper panels). Nevertheless,

the difference in line emissivity for two luminosity cases decreases with the increasing cloud density (towards lower panels).

4.3 Dependence on cloud column density

For the single thick cloud consideration, the increase of cloud column density implies that more cold matter is added on the back, non-illuminated side of the cloud. Therefore, the line emissivity increases with the column density, but only when the starting gas density is relatively low, as seen in Figs. 12 and 13. On the other hand, by increasing the column density, the total cloud size increases together with the line luminosity, which is demonstrated in Figs. 16 and 17, where the single cloud structure is presented for the high Cen A luminosity case and low starting density

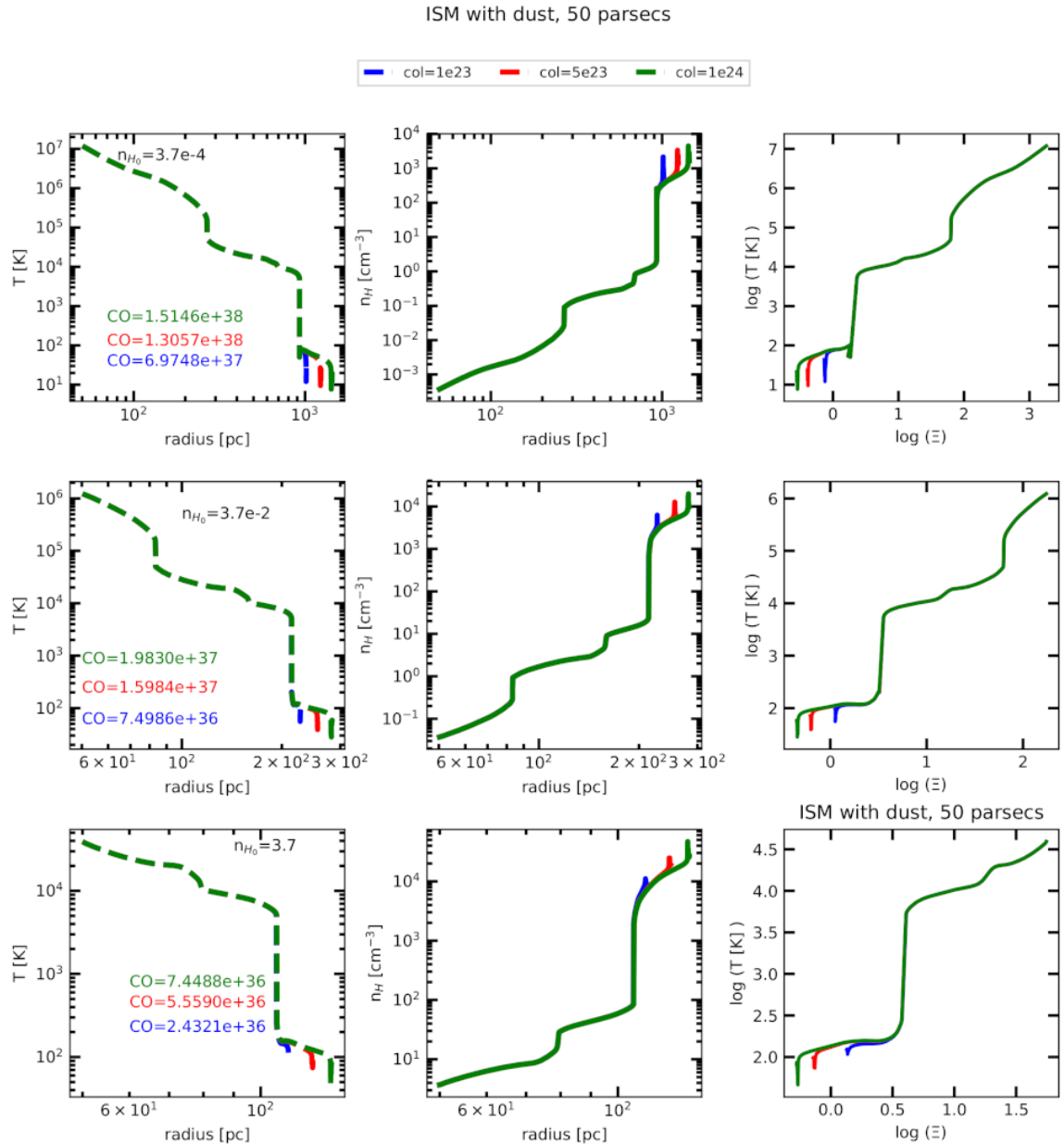


Figure 11. Same as in Fig. 9, but for an inner radius of 50 pc.

$n_{H_0} = 3.7 \times 10^{-4} \text{ cm}^{-3}$ for two distances from the SMBH: 10 and 50 pc respectively. Different line styles represent cases with increasing column density, and clearly show the process of adding more material on the back side of the cloud. This material is becoming cold, dust dominated and radially more extended. In each case, the outer size of the cloud is marked by a vertical line, and integrated CO line luminosity is shown.

Both figures show how the molecular gas layers are formed on the back, non-illuminated side of the clouds. In the case when the illuminated cloud surface is located at 10 pc, the molecular layer starts at 269.15 pc and it has a geometrical extension equal to 155.36 pc. But the estimated CO line luminosity is one order of magnitude below the observed value. The overall properties of such

cloud and computed line luminosities are presented in Tab. 3 in the sixth column.

The situation changes when the cloud is located at 50 pc from the SMBH. Fig. 17 shows the extension of dust for this case, when the observed L_{CO} luminosity is almost fully reproduced. The modelled luminosities of several lines for this model are listed in Tab. 3 in the seventh column. We found, that in order to reproduce the observed CO line emissivity, the thickness of dusty material should be about 419 pc, which is 22'', located around 1020 pc (55''). In both cases of clouds considered here, the hot plasma extends within 184 pc, which agrees with the *Chandra* observations.

The above results prompted us to propose a 3-D model of the hot plasma and molecular gas distribution, which is consistent with the *Chandra* observations and with the ALMA observed

Table 3. The most intensive line luminosities measured by ALMA from the images given in Figs. 2, 3, 4. First two columns display the line transition and its frequency, while the line luminosities integrated over the circular surface with radius $4.5''$ are given in column 3. The critical densities above which lines are visible are displayed in column 4. Corresponding wavelength of each line is given in column 5. The line luminosities obtained from CLOUDY computations for two cloud locations, 10 and 50 pc, are listed in the columns 6 and 7 respectively.

Line Name	Observations			Modelling		
	Freq. ALMA [GHz]	Lum. ALMA [erg s ⁻¹]	n_{crit} [cm ⁻³]	Wavelengtht [μm]	Lum. CLOUDY [erg s ⁻¹]	Lum. CLOUDY [erg s ⁻¹]
					$n_{\text{H}_0} = 3.7 \times 10^{-4} \text{ cm}^{-3}$	$n_{\text{H}_0} = 3.7 \times 10^{-4} \text{ cm}^{-3}$
CO (1 – 0)	115.271202	1.97×10^{38}	1×10^3	2600.05	3.3678×10^{37}	1.5146×10^{38}
13CO (1 – 0)	110.201354	1.97×10^{37}				
CS (2 – 1)	97.980953	1.69×10^{37}	1.3×10^5	3058.86	2.4275×10^{37}	9.3450×10^{37}
HCN (3 – 2)	265.886431	9.87×10^{37}	1.4×10^7	1127.22	1.3457×10^{38}	5.8938×10^{38}
HCO+ (3 – 2)	267.557633	1.06×10^{38}	1.6×10^6	1120.18	3.1272×10^{37}	6.3693×10^{37}
HNC (3 – 2)	271.981111	6.24×10^{37}	5.1×10^6	1101.95	2.5199×10^{38}	9.4087×10^{38}

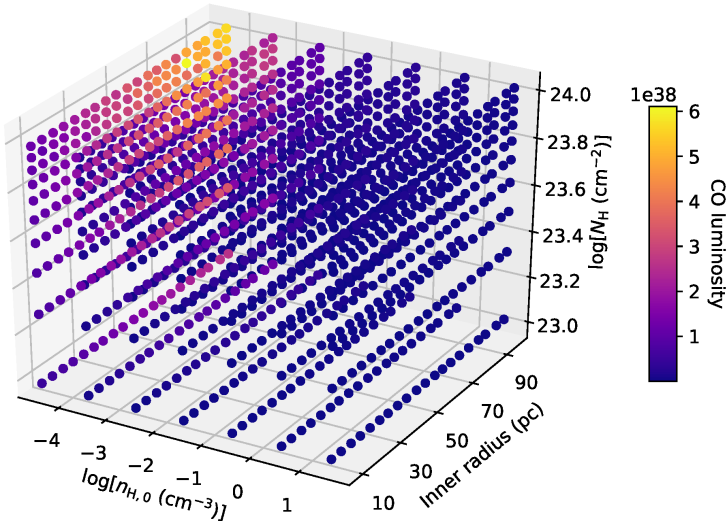


Figure 12. 3D plot of CO (1 – 0) line emission computed in CLOUDY as a function of parameters: gas density, inner radius and, the column density.

CO line. Assuming a spherically symmetric model, the hot plasma, with temperature above 10^6 K is located in the innermost region of $10''$, which agrees with our data presented in Fig. 1. With increasing radial distance the temperature of matter decreases and dusty molecular material starts to be visible. When projected onto the sky, we obtain the a line luminosity similar to that observed within the Reg1 on Fig. 5, but the most dust concentration is further out at $55''$, which is consistent with emission from Reg4, and farther out of Reg3 in this figure.

5 DISCUSSION AND CONCLUSIONS

We explored the conditions for the onset of thermal instability near a SMBH residing in the core of the Cen A galaxy. Such an instability can arise when the gas is illuminated by a strong radiation field from the nucleus. With this aim, we analysed *Chandra* X-ray observations and ALMA data covering the mm band, focusing in both cases on the inner $10''$ region (184 pc) of the galaxy. The images show an overlap of the hot X-ray emitting plasma with the cold CO-emitting and dusty material. The object has been described in

the literature before, but with the focus either on the X-ray emission and jet properties (e.g. Evans et al. 2004; Snios et al. 2019), or on the dynamics, the properties of the cold gas well measured through observations of the molecular lines, and the role of star formation activity (e.g. Espada et al. 2017; McCoy et al. 2017; Espada et al. 2019). Our goal was to model the interaction of the hot plasma and the cold material and to verify whether thermal instability leads to spontaneous formation of this multi-phase environment.

In order to understand the relevant processes we used one SED of broad-band emission from the very inner region of Cen A available in the literature. We considered two luminosity states that differ by a factor of 70, which accounts for the fact that some emission may originate from the non-thermal jet and may be strongly boosted, and for the effect of intrinsic variability of the source. We performed our photoionization calculations under the assumption of all clouds satisfying the constant pressure approximation and the gas including heavy elements with ISM and Solar abundances.

We demonstrated that thermal instability is indeed able to generate the multi-phase medium, where the hot X-ray phase with temperature $\sim 10^6$ K stays in pressure equilibrium with the partially

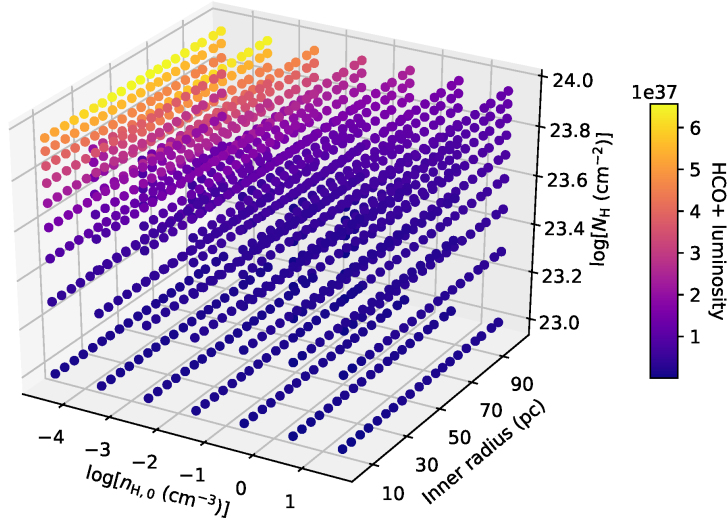


Figure 13. 3D plot of HCO+ (3 – 2) line emission computed in CLOUDY as a function of parameters: gas density, inner radius and, the column density.

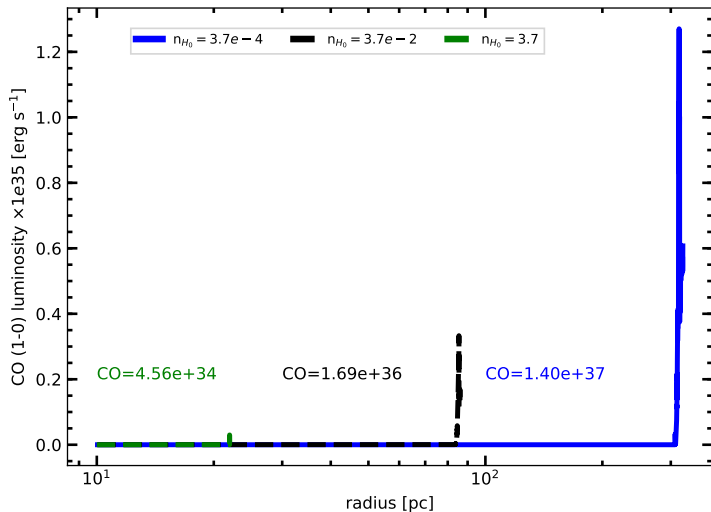


Figure 14. CO (1 – 0) luminosity as a function of radial distance. Emission for three cases of initial densities $n_{H_0} = 3.7 \times 10^{-4}$, 3.7×10^{-2} and 3.7 cm^{-3} are shown. Total luminosity is obtained by integrating the luminosity over the whole radii.

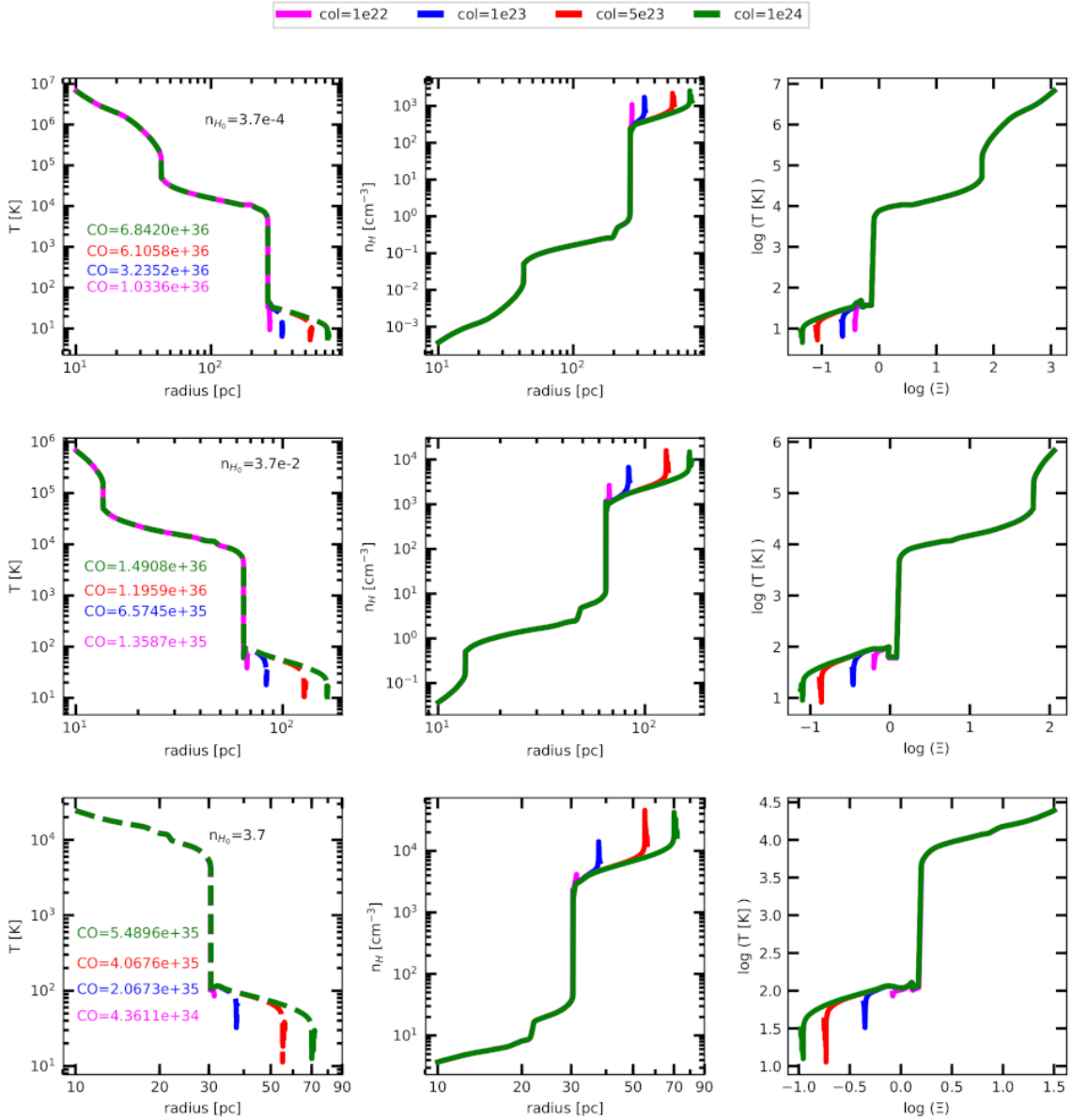
ionized gas of temperature $\sim 10^4$ K that emits the H_α spectral line. Nevertheless, the cold dust of temperature $T < 100$ K, responsible for the CO emission detected by ALMA, cannot co-exist with the X-ray emitting plasma but it could co-exist with the H_α emitting gas at $\log \Xi = -5$. This is a factor 10^5 difference in the allowed level of irradiation. However, we note that this statement is correct for optically thin gas, which is also the assumption behind the computations of our equilibrium curves.

With the advanced photoionization CLOUDY computations we were able to search systematically over a wide parameter space. In this way we found the conditions for clouds of relatively low density, which can reproduce the observed CO line emission that reaches 1.51×10^{38} erg s $^{-5}$. This flux is achieved for clouds located at ~ 50 pc and further away from the nucleus. The modelled luminosities of all other observed lines (see Tab. 3) are higher than the

observed ones, which we explain by the effect of shielding. Next, for the cloud located closer to the nucleus, the modeled CO line is one order of magnitude lower than the observed one, but the other lines are again overestimated.

The CO line is the most important from the observational point of view, and we thus concentrate towards reproducing its modelled luminosity. Note, that such a line may only be produced in the high-luminosity state of Cen A, since CO line luminosity decreases as the bolometric luminosity decreases.

From our modelling, we have shown that the best distribution of matter that correctly reproduces the data is the 3-D cloud where the hot plasma extends up to $r_{\max} \simeq 200$ pc from the centre, which agrees with *Chandra* observations within 10''. When the temperature drops below 1×10^6 K, we cannot consider this environment as a hot X-ray emitting medium. Instead, we start seeing the emer-

ISM with dust, 10 parsecs, luminosity $1.43 \times 10^{41} \text{ ergs}^{-1}$ **Figure 15.** The same as in Fig. 9 but for the lower radiation luminosity of $1.43 \times 10^{41} \text{ erg s}^{-1}$.

gence of H α emitting clouds due to TI at $r_{\min} \simeq 200 \text{ pc}$ in the dust-less region, and $r_{\min} \simeq 1020 \text{ pc}$ in the dusty region (for the cloud of starting density $n_{H_0} = 3.7 \times 10^{-4} \text{ cm}^{-3}$ located at 50 pc).

A fraction of $1 \times 10^4 \text{ K}$ material is associated with the jet, and this means that we do not expect dust to be present in the jet region. Dust was probably destroyed in the outflow in course of the accretion process. Therefore, the dusty material is a part of the spherical shell located outside the jet viewing angle; it should have geometrical thickness of $\sim 419 \text{ pc}$, and it should be placed at $\sim 1020 \text{ pc}$ from the nucleus. Such a location implies that we see the very inner region of Cen A as a projected image on the sky through the dusty material. The location of the dust lanes further outside the nucleus is confirmed by the ALMA total map presented in Fig. 5, where the most luminous CO line emission is up $50''$ on the North

East side, and even $60''$ on the South West side of the disk like shape.

Our choice of CLOUDY software for modelling did not allow for deep and focused analysis of the molecular lines as could be done by using specialized softwares, for example radiative transfer codes like RADEX (van der Tak et al. 2007; Kawamuro et al. 2019, 2020), or the KOSMA-tau code (Stutzki et al. 1998), which combines the modelling of individual spherical clumps in an isotropic UV field assuming a fractal structure of the ISM. Some upgraded versions allow the user to even include the cosmic ray heating and mechanical heating by turbulence and shocks or X-ray interaction with a partially ionized dusty medium (e.g. Meijerink & Spaans 2005; Meijerink et al. 2006, 2007; Kazandjian et al. 2012, 2016). On the other hand, these codes do not consider X-ray emitting hot

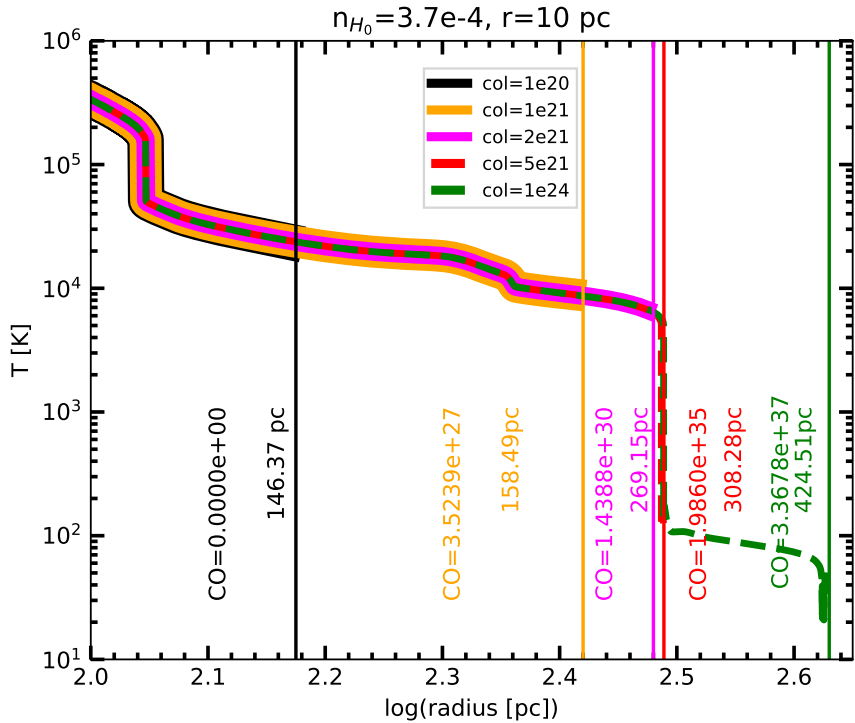


Figure 16. Length scales of CO (1 – 0) emission for various column densities given in the panel box. The model is computed for the gas density: 3.7×10^{-4} located at the inner radius 10 pc. For each case the cloud outer radius is marked by a vertical line. The resulting cloud sizes and CO (1 – 0) line luminosities are displayed near each vertical line.

plasma where Comptonization plays a dominant role, thus only CLOUDY allows us to cover the complete temperature range from tens of K to 10^8 K, i.e. to the temperature saturation at the inverse Compton temperature value for a given spectral shape of the incident continuum.

Our results confirm the existence of the multi-phase medium in Cen A, including the hot X-ray emitting phase, as shown previously in two other sources: Sgr A* and M60-UCD1, the latter being an ultra-compact dwarf galaxy (Czerny et al. 2013; Różańska et al. 2014; Kunneriath et al. 2014; Różańska et al. 2017). We postulate here that active galaxies have enough power to produce a strong radiation field which then photoionizes the gas around their SMBHs. Such illumination enhances the classical TI, where under the usual constant pressure assumption the hot and cold gas can co-exist. Dusty gas is moved outside the nucleus, most probably due to strong evaporation at the hot phase. The location of these phases agrees with currently available high-resolution images by X-ray and infrared telescopes. As the TI develops, it helps cold clumps to survive within the surrounding hot medium and drives them toward the central SMBH (Barai et al. 2011, 2012), thus enhancing the mass accretion rate during episodes of clumps disruption and inflow.

ACKNOWLEDGMENTS

This paper is based on the following ALMA data: ADS/JAO.ALMA#2015.1.00483.S. ALMA is a partnership of ESO (representing its member states), NSF (USA) and NINS

(Japan), together with NRC (Canada) and NSC and ASIAA (Taiwan) and KASI (Republic of Korea), in cooperation with the Republic of Chile. The Joint ALMA Observatory is operated by ESO, AUI/NRAO, and NAOJ. The research was supported by Czech Science Foundation No. 19-05599Y (AB and PB) and No. 19-01137J (VK), and the EU-ARC.CZ Large Research Infrastructure grant project LM2018106 of the Ministry of Education, Youth and Sports of the Czech Republic (AB). The research was also supported by Polish National Science Center grants No. 2015/17/B/ST9/03422, 2015/18/M/ST9/00541 (TPA and AR), 2016/23/B/ST9/03123, 2018/31/G/ST9/03224 (AGM), 2017/26/A/ST9/00756 (BCZ). BDM acknowledges support from the European Union’s Horizon 2020 research and innovation programme under the Marie Skłodowska-Curie grant agreement No. 798726. TPA acknowledges the Nicolaus Copernicus Astronomical Center of the Polish Academy of Sciences (NCAC PAS) for its hospitality during his stay in Warsaw.

REFERENCES

- Abdo A. A., et al., 2010, *ApJ*, **719**, 1433
- Adhikari T. P., 2019, Photoionization Modelling as a Density Diagnostic of Line Emitting/Absorbing Regions in Active Galactic Nuclei. Springer International Publishing, doi:10.1007/978-3-030-22737-1
- Adhikari T. P., Różańska A., Sobolewska M., Czerny B., 2015, *ApJ*, **815**, 83
- Adhikari T. P., Hryniwicz K., Różańska A., Czerny B., Ferland G. J., 2018, *ApJ*, **856**, 78

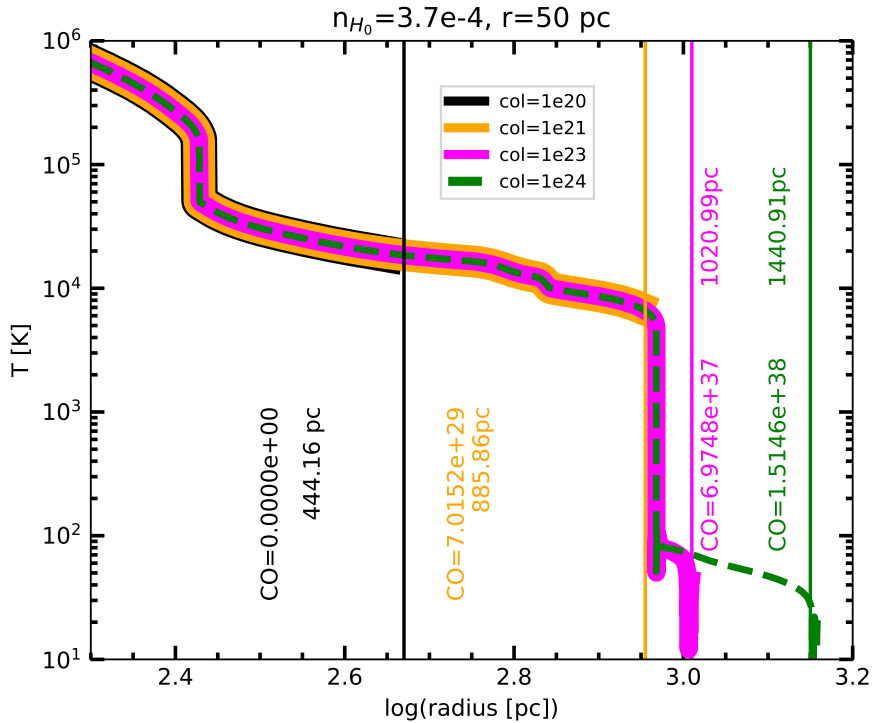


Figure 17. Same as Fig. 16, but for $r = 50$ pc.

Adhikari T. P., Różańska A., Hryniwicz K., Czerny B., Behar E., 2019, *ApJ*, **881**, 78

Astropy Collaboration et al., 2013, *A&A*, **558**, A33

Barai P., Proga D., Nagamine K., 2011, *MNRAS*, **418**, 591

Barai P., Proga D., Nagamine K., 2012, *MNRAS*, **424**, 728

Baskin A., Laor A., Stern J., 2014, *MNRAS*, **438**, 604

Burke M. J., et al., 2013, *ApJ*, **766**, 88

Cappellari M., Neumayer N., Reunanen J., van der Werf P. P., de Zeeuw P. T., Rix H. W., 2009, *MNRAS*, **394**, 660

Cox D. P., 2005, *ARA&A*, **43**, 337

Croston J. H., et al., 2009, *MNRAS*, **395**, 1999

Czerny B., Kunneriath D., Karas V., Das T. K., 2013, *A&A*, **555**, A97

Dannen R. C., Proga D., Waters T., Dyda S., 2020, *ApJ*, **893**, L34

Duras F., et al., 2020, *A&A*, **636**, A73

Espada D., et al., 2009, *ApJ*, **695**, 116

Espada D., et al., 2010, *ApJ*, **720**, 666

Espada D., et al., 2017, *ApJ*, **843**, 136

Espada D., et al., 2019, *ApJ*, **887**, 88

Evans I. N., Koratkar A. P., 2004, *ApJ*, **617**, 209

Evans D. A., Kraft R. P., Worrall D. M., Hardcastle M. J., Jones C., Forman W. R., Murray S. S., 2004, *ApJ*, **612**, 786

Fanaroff B. L., Riley J. M., 1974, *MNRAS*, **167**, 31P

Ferland G. J., et al., 2017, *Rev. Mex. Astron. Astrofis.*, **53**, 385

Field G. B., 1965, *ApJ*, **142**, 531

Fruscione A., et al., 2006, in Society of Photo-Optical Instrumentation Engineers (SPIE) Conference Series. p. 62701V, doi:10.1117/12.671760

Fukazawa Y., et al., 2011, *ApJ*, **743**, 124

Fürst F., et al., 2016, *ApJ*, **819**, 150

Goodger J. L., et al., 2010, *ApJ*, **708**, 675

H. E. S. S. Collaboration et al., 2018, *A&A*, **619**, A71

Hardcastle M. J., Worrall D. M., Kraft R. P., Forman W. R., Jones C., Murray S. S., 2003, *ApJ*, **593**, 169

Hardcastle M. J., et al., 2007, *ApJ*, **670**, L81

Harris G. L. H., Rejkuba M., Harris W. E., 2010, *Publ. Astron. Soc. Australia*, **27**, 457

Harrison F. A., et al., 2013, *ApJ*, **770**, 103

Hess C. J., Kahn S. M., Paerels F. B. S., 1997, *ApJ*, **478**, 94

Israel F. P., 1998, *A&ARv*, **8**, 237

Jourdain E., et al., 1993, *ApJ*, **412**, 586

Kawamuro T., Izumi T., Imanishi M., 2019, *PASJ*, **71**, 68

Kawamuro T., Izumi T., Onishi K., Imanishi M., Nguyen D. D., Baba S., 2020, arXiv e-prints, p. arXiv:2004.09394

Kazandjian M. V., Meijerink R., Pelupessy I., Israel F. P., Spaans M., 2012, *A&A*, **542**, A65

Kazandjian M. V., Pelupessy I., Meijerink R., Israel F. P., Spaans M., 2016, *A&A*, **595**, A125

Kinzer R. L., et al., 1995, *ApJ*, **449**, 105

Kraft R. P., Vázquez S. E., Forman W. R., Jones C., Murray S. S., Hardcastle M. J., Worrall D. M., Churazov E., 2003, *ApJ*, **592**, 129

Kraft R. P., et al., 2008, *ApJ*, **677**, L97

Krajnović D., Sharp R., Thatte N., 2007, *MNRAS*, **374**, 385

Krolik J. H., McKee C. F., Tarter C. B., 1981, *ApJ*, **249**, 422

Kunneriath D., Czerny B., Karas V., Das T. K., 2014, in Sjouwerman L. O., Lang C. C., Ott J., eds, IAU Symposium Vol. 303, The Galactic Center: Feeding and Feedback in a Normal Galactic Nucleus. pp 320–321, doi:10.1017/S1743921314000830

Loenen A. F., Baan W. A., Spaans M., 2007, in Chapman J. M., Baan W. A., eds, IAU Symposium Vol. 242, Astrophysical Masers and their Environments. pp 462–466 (arXiv:0709.3423), doi:10.1017/S1743921307013609

Marconi A., Pastorini G., Pacini F., Axon D. J., Capetti A., Macchetto D., Koekemoer A. M., Schreier E. J., 2006, *A&A*, **448**, 921

Markowitz A., et al., 2007, *ApJ*, **665**, 209

McCoy M., et al., 2017, *ApJ*, **851**, 76

McMullin J. P., Waters B., Schiebel D., Young W., Golap K., 2007, in Shaw R. A., Hill F., Bell D. J., eds, Astronomical Society of the Pacific Con-

ference Series Vol. 376, Astronomical Data Analysis Software and Systems XVI, p. 127

Meijerink R., Spaans M., 2005, *A&A*, **436**, 397

Meijerink R., Spaans M., Israel F. P., 2006, *ApJ*, **650**, L103

Meijerink R., Spaans M., Israel F. P., 2007, *A&A*, **461**, 793

Neumayer N., 2010, *Publ. Astron. Soc. Australia*, **27**, 449

Neumayer N., Cappellari M., Reunanen J., Rix H. W., van der Werf P. P., de Zeeuw P. T., Davies R. I., 2007, *ApJ*, **671**, 1329

Quataert E., 2004, *ApJ*, **613**, 322

Radomski J. T., et al., 2008, *ApJ*, **681**, 141

Rejkuba M., 2004, *A&A*, **413**, 903

Risaliti G., Elvis M., Nicastro F., 2002, *ApJ*, **571**, 234

Rivers E., Markowitz A., Rothschild R., 2011, *ApJ*, **742**, L29

Rothschild R. E., et al., 2006, *ApJ*, **641**, 801

Rothschild R. E., Markowitz A., Rivers E., Suchy S., Pottschmidt K., Kadler M., Müller C., Wilms J., 2011, *ApJ*, **733**, 23

Różańska A., Czerny B., 1996, *Acta Astron.*, **46**, 233

Różańska A., Goosmann R., Dumont A.-M., Czerny B., 2006, *A&A*, **452**, 1

Różańska A., Czerny B., Kunneriath D., Adhikari T. P., Karas V., Mościbrodzka M., 2014, *MNRAS*, **445**, 4385

Różańska A., Kunneriath D., Czerny B., Adhikari T. P., Karas V., 2017, *MNRAS*, **464**, 2090

Shirley Y. L., 2015, *PASP*, **127**, 299

Silge J. D., Gebhardt K., Bergmann M., Richstone D., 2005, *AJ*, **130**, 406

Silich S., Tenorio-Tagle G., Rodríguez-González A., 2004, *ApJ*, **610**, 226

Silich S., Tenorio-Tagle G., Hueyotl-Zahuantitla F., 2008, *ApJ*, **686**, 172

Snios B., et al., 2019, *ApJ*, **871**, 248

Solomon P. M., Downes D., Radford S. J. E., Barrett J. W., 1997, *ApJ*, **478**, 144

Steinle H., et al., 1998, *A&A*, **330**, 97

Stutzki J., Bensch F., Heithausen A., Ossenkopf V., Zielinsky M., 1998, *A&A*, **336**, 697

Tarter C. B., Tucker W. H., Salpeter E. E., 1969, *ApJ*, **156**, 943

Tingay S. J., Lenc E., 2009, *AJ*, **138**, 808

Tingay S. J., Preston R. A., Jauncey D. L., 2001, *AJ*, **122**, 1697

Waters T., Proga D., 2019, *ApJ*, **875**, 158

Worrall D. M., et al., 2008, *ApJ*, **673**, L135

van der Tak F. F. S., Black J. H., Schöier F. L., Jansen D. J., van Dishoeck E. F., 2007, *A&A*, **468**, 627